

Review

# Facet-Dependent Reactivity of Ceria Nanoparticles Exemplified by CeO<sub>2</sub>-Based Transition Metal Catalysts: A Critical Review

Michalis Konsolakis \*  and Maria Lykaki

Industrial, Energy and Environmental Systems Lab (IEESL), School of Production Engineering and Management, Technical University of Crete, GR-73100 Chania, Greece; mlykaki@isc.tuc.gr

\* Correspondence: mkonsol@pem.tuc.gr; Tel.: +30-2821-037682

**Abstract:** The rational design and fabrication of highly-active and cost-efficient catalytic materials constitutes the main research pillar in catalysis field. In this context, the fine-tuning of size and shape at the nanometer scale can exert an intense impact not only on the inherent reactivity of catalyst's counterparts but also on their interfacial interactions; it can also opening up new horizons for the development of highly active and robust materials. The present critical review, focusing mainly on our recent advances on the topic, aims to highlight the pivotal role of shape engineering in catalysis, exemplified by noble metal-free, CeO<sub>2</sub>-based transition metal catalysts (TMs/CeO<sub>2</sub>). The underlying mechanism of facet-dependent reactivity is initially discussed. The main implications of ceria nanoparticles' shape engineering (rods, cubes, and polyhedra) in catalysis are next discussed, on the ground of some of the most pertinent heterogeneous reactions, such as CO<sub>2</sub> hydrogenation, CO oxidation, and N<sub>2</sub>O decomposition. It is clearly revealed that shape functionalization can remarkably affect the intrinsic features and in turn the reactivity of ceria nanoparticles. More importantly, by combining ceria nanoparticles (CeO<sub>2</sub> NPs) of specific architecture with various transition metals (e.g., Cu, Fe, Co, and Ni) remarkably active multifunctional composites can be obtained due mainly to the synergistic metalceria interactions. From the practical point of view, novel catalyst formulations with similar or even superior reactivity to that of noble metals can be obtained by co-adjusting the shape and composition of mixed oxides, such as Cu/ceria nanorods for CO oxidation and Ni/ceria nanorods for CO<sub>2</sub> hydrogenation. The conclusions derived could provide the design principles of earth-abundant metal oxide catalysts for various real-life environmental and energy applications.

**Keywords:** ceria morphological effects; shape effects in catalysis; CeO<sub>2</sub>-based catalysts; CO oxidation; N<sub>2</sub>O decomposition; CO<sub>2</sub> hydrogenation



**Citation:** Konsolakis, M.; Lykaki, M. Facet-Dependent Reactivity of Ceria Nanoparticles Exemplified by CeO<sub>2</sub>-Based Transition Metal Catalysts: A Critical Review. *Catalysts* **2021**, *11*, 452. <https://doi.org/10.3390/catal11040452>

Academic Editors: Stanisław Waclawek, Dionysios (Dion) D. Dionysiou, Andrzej Kudelski and Jochen A. Lauterbach

Received: 22 March 2021

Accepted: 30 March 2021

Published: 31 March 2021

**Publisher's Note:** MDPI stays neutral with regard to jurisdictional claims in published maps and institutional affiliations.



**Copyright:** © 2021 by the authors. Licensee MDPI, Basel, Switzerland. This article is an open access article distributed under the terms and conditions of the Creative Commons Attribution (CC BY) license (<https://creativecommons.org/licenses/by/4.0/>).

## 1. Introduction

Catalysis has gained ongoing attention from academic and industrial community, since it is massively involved in numerous energy and environmental processes, including, among others, the manufacture of value-added fuels and chemicals, hydrocarbons processing, fuel cell applications, photocatalytic degradation, abatement of hazardous substances, etc. To this end, the development of cost-efficient catalysts with improved activity and durability constitutes the main research pillar in the field of catalysis [1–8].

Although, noble metals (NMs) hold an integral role in catalysis for chemical bond activation and formation, their scarcity and high cost constitutes a major and inherent drawback. In this regard, the development of catalysts by combining the low cost with the high activity is a major driving force in contemporary research [2–6,8–10]. In this regard, however, a critical question arises: Is it feasible to adjust the surface chemistry of earth-abundant but relatively inactive materials in order to exhibit similar or ever superior performance to that of NMs? On account to the enormous progress so far accomplished on nano-synthesis, surface/interface functionalization and catalyst promotion fields, the answer to this question is definitely yes, as recently demonstrated [11–27].

Metal oxides, composed of earth-abundant transition metals (TMs) have gained particular attention towards replacing the rare and costly NMs, owing to their unique characteristics, such as improved redox properties and thermal stability [2,3,5,6,9,28–46]. More importantly, through admixing different metal oxides (MOs) in an exact proportion, mixed metal oxides (MMOs) can be obtained with unique physicochemical properties, which are mainly linked to interfacial phenomena. In particular, MOs-based transition metals have received particular attention due to the distinctive chemisorption ability of TMs, related to their partially filled d-shells [47,48]. Moreover, several reducible oxides (e.g., CeO<sub>2</sub>, ZnO, and TiO<sub>2</sub>), could serve as TMs supporting carriers, exerting a beneficial impact on the inherent activity through peculiar metal–support interactions [16,25,41,49–54].

Among the different MOs, cerium oxide or ceria has gained tremendous interest in heterogeneous catalysis due to its exceptional redox properties driven by the high oxygen mobility and the rapid redox interplay between Ce<sup>3+</sup> and Ce<sup>4+</sup> [2,9,21,23,55–57]. In addition to these physicochemical advantages of cerium oxide, its average 2020 price stands at very low levels (ca. 1815 USD/metric ton), with a relative cost trend of ZrO<sub>2</sub> > ZnO > SiO<sub>2</sub> > TiO<sub>2</sub> > CeO<sub>2</sub>, revealing the economic benefits of ceria-based catalytic materials [58]. Furthermore, the cost of base middle–late 3d metals, such as Cu, Ni, is about 3 to 4 orders of magnitude lower as compared to NMs, rendering extremely attractive, from a financial perspective, the development of ceria-based transition metal catalysts. More importantly, the combination of reducible oxides (e.g., CeO<sub>2</sub>) with TMs (e.g., Fe, Co, Ni, and Cu) could offer novel catalyst formulations with exceptional properties, arising mainly from the multifaceted electronic and geometric interactions amongst the different counterparts [14,16,25,27,41,49–54,59,60]. In this respect, it was recently appraised on account of both experimental and theoretical studies that various interconnected phenomena could be at work at metal–support interface, which in turn exert a profound influence on the catalytic activity, including the following [14,25,27,41,59–61]:

- i. Electronic perturbations linked to bonding interactions between TMs and ceria nanoparticles
- ii. Facilitation of oxygen vacancies' formation resulting in enhanced reducibility and oxygen exchange kinetics
- iii. High intrinsic activity of interfacial sites

However, it is well-known today—thanks to the huge progress in cutting-edge characterization techniques—that the individual characteristics of catalyst's counterparts can notably affect not only their own activity but also the interaction between them with great consequences in catalysis. More specifically, by adjusting the geometrical and electronic features of the different counterparts through suitable synthetic and promotional routes highly active materials are obtained [12–19,21,22,24,27,56,62–74]. Table 1 depicts at a glance, the main physicochemical modifications that can be induced by adjusting each of the aforementioned parameters.

The recent advances in relation to the role of shape, size and electronic modulation on inherent reactivity and interfacial interactions were recently reviewed on the basis of CuO<sub>x</sub>/CeO<sub>2</sub> oxides [13]. It became evident that by appropriately adjusting the aforementioned parameters, highly active composites can be obtained with a comparable or even superior performance as compared to NMs-based composites. The present critical review focuses on the particular role of ceria shape on the physicochemical characteristics and the catalytic performance of bare CeO<sub>2</sub>, as well as of TMs/CeO<sub>2</sub> composites, with particular emphasis on our recent efforts in the field. The synthesis procedure of bare CeO<sub>2</sub> nanoparticles of well-defined morphology, i.e., nanocubes (NC), nanorods (NR), and nanopolyhedra (NP), as well as of the corresponding ceria-based TMs (Fe, Co, Ni, and Cu) is initially described. A thorough characterization study by applying various characterization techniques is next presented for single CeO<sub>2</sub> and TMs/CeO<sub>2</sub> samples so as to disclose the effect of ceria shape on the intrinsic properties and interfacial phenomena. Finally, the implications of ceria shape engineering will be exemplified on the basis of CO oxidation, N<sub>2</sub>O decomposition, and CO<sub>2</sub> hydrogenation reactions over TMs/ceria catalysts.

**Table 1.** Adjusted parameters and their implications in the physicochemical characteristics of metal oxides.

Adjusted Parameter	Main Implications in Physicochemical Properties
Composition (e.g., binary or ternary MOs)	surface area; structural characteristics
Size (e.g., metal particles of nanometer size)	surface area; electronic environment; coordination environment; structural defects
Shape (e.g., nanorods and nanocubes)	energy formation of anionic vacancies; redox features
Electronic state (e.g., alkali addition)	work function; redox characteristics
Chemical state (e.g., incorporation of rGO)	redox properties; structural defects; electronic environment

## 2. Synthesis and Characterization of CeO<sub>2</sub> NPs of Different Morphology

Concerning the preparation of ceria nanoparticles, numerous synthetic routes have been employed, such as thermal decomposition, precipitation, sol–gel, solution combustion, surfactant or template-assisted method, hydrothermal or alcohothermal method, microemulsion, sonochemical, microwave-assisted synthesis, etc. [75–99]. Among the different preparation techniques, the hydrothermal method has been widely employed, owing to the short reaction time, the simple precursor compounds utilized, the homogeneous morphology and the development of nanoparticles with well-defined shapes, such as wires, polyhedra, rods, and cubes [71,75,76,81,82,95,100–114] (Figure 1).

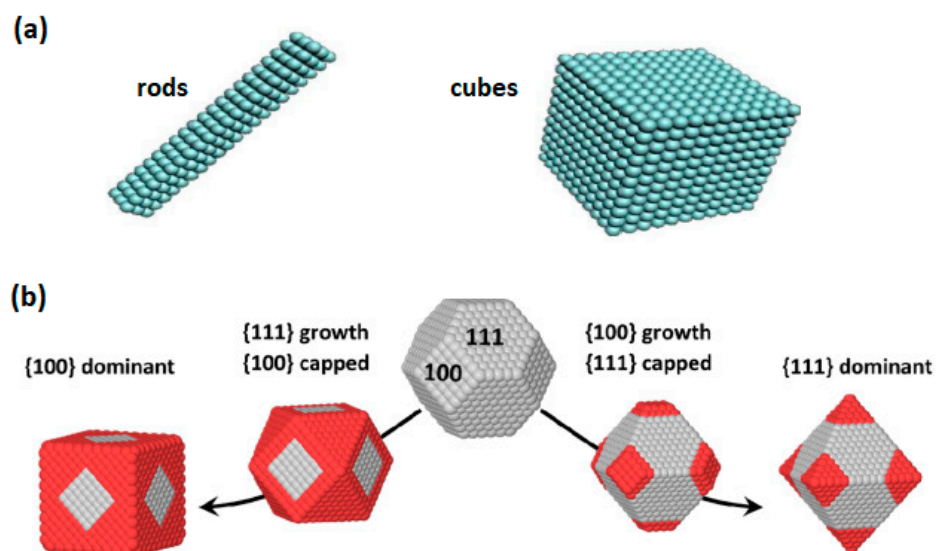


**Figure 1.** (a) Model shapes of rods and cubes. Reproduced with permission from Reference [115]. Copyright© 2018, Elsevier. (b) Model shapes illustrating an anisotropic growth process starting from a truncated cuboctahedron shape. Protecting the {111} facets by using a capping agent results in the growth of {100} facets until they disappear and only {111} facets remain on the surface (octahedral shape). The opposite would result in cubic nanoparticles NPs with only {100} facets. Reproduced with permission from Reference [116]. Copyright© 2015, Elsevier.

In our recent works [33–35,38,39,75], the hydrothermal method was successfully used in order to prepare three distinct ceria morphologies of well-defined shape, i.e., nanocubes (NC), nanorods (NR), and nanopolyhedra (NP), which are then employed as supporting carriers for various transition metal catalysts (Fe, Co, Ni, and Cu). Figure 2 schematically

illustrates the procedure followed for the preparation of CeO<sub>2</sub>-NP, CeO<sub>2</sub>-NR and CeO<sub>2</sub>-NC. Briefly, suitable amounts of cerium nitrate hexahydrate (Ce(NO<sub>3</sub>)<sub>3</sub>·6H<sub>2</sub>O) and sodium hydroxide (NaOH) were firstly dissolved in deionized H<sub>2</sub>O, mixed under continuous stirring for 1 h, and finally aged at 180 °C for 24 h (for cubes) or at 90 °C (for rods and polyhedra). The precipitates obtained by centrifugation were washed several times with deionized H<sub>2</sub>O and finally with C<sub>2</sub>H<sub>5</sub>OH, to prevent agglomeration. The obtained precipitate was finally dried and calcined for 2 h, at 500 °C.

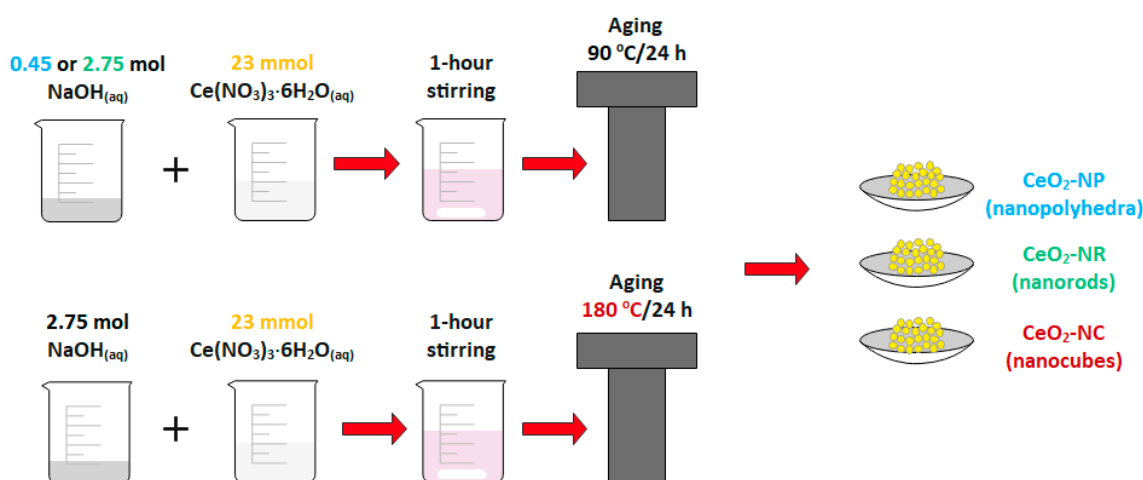


**Figure 2.** Schematic illustration of synthetic procedure of ceria nanoparticles of different shape (nanocubes = NC, nanorods = NR, and nanopolyhedra = NP).

Ceria-based transition metals, i.e., Fe, Co, Ni, and Cu, were next prepared through wet impregnation, employing the corresponding aqueous nitrate precursors. In all cases the metal/Ce atomic ratio was kept constant at 0.25. Suspensions were dried at 90 °C and finally calcined for 2 h, at 500 °C. The as-prepared materials are denoted for convenience as M/CeO<sub>2</sub>-NX, where M = Cu, Co, Ni, and Fe, whereas NX stands for nanorods (NR), nanocubes (NC) and nanopolyhedra (NP).

Both bare CeO<sub>2</sub>-NX and M/CeO<sub>2</sub>-NX nanocomposites were characterized by various techniques in order to gain insight into the effect of ceria morphology, metal nature and metal–support interactions on the textural, morphological, structural, and redox properties. In particular, the following characterization methods were employed: N<sub>2</sub> adsorption-desorption (BET method), X-ray diffraction (XRD), transmission electron microscopy (TEM), temperature programmed reduction (TPR), X-ray photoelectron spectroscopy (XPS), and in situ Raman spectroscopy, as described in detail elsewhere [34].

### 3. Ceria Shape Effects on the Structural Defects and Redox Properties

In this part, the impact of distinct morphology on the physicochemical characteristics of bare ceria nanoparticles is initially discussed. Figure 3 shows indicative TEM images of ceria nanorods, nanopolyhedra, and nanocubes. The CeO<sub>2</sub>-NR sample (Figure 3a,d) shows a rod-like morphology with a length from 25 to 200 nm. In the case of CeO<sub>2</sub>-NC (Figure 3c,f), a well-defined cube-like morphology is obtained (of about 20–30 nm), whereas nanopolyhedra of irregular size/shape are observed for CeO<sub>2</sub>-NP (Figure 3b,e).

For the sake of clarity, the main textural and structural characteristics of ceria nanoparticles are summarized in Table 2. The following order, in relation to BET area, was disclosed: NC (40 m<sup>2</sup>/g) < NR (92 m<sup>2</sup>/g) < NP (109 m<sup>2</sup>/g). The average crystallite diameter of CeO<sub>2</sub> phase, calculated by applying Scherrer equation on the XRD diffractions, follows the reverse order, i.e., NP (9.5 nm) < NR (13.2 nm) < NC (19.2 nm). Among the different ceria nanostructures, ceria nanocubes exhibit the lowest BET surface area, along with the highest mean particle size.

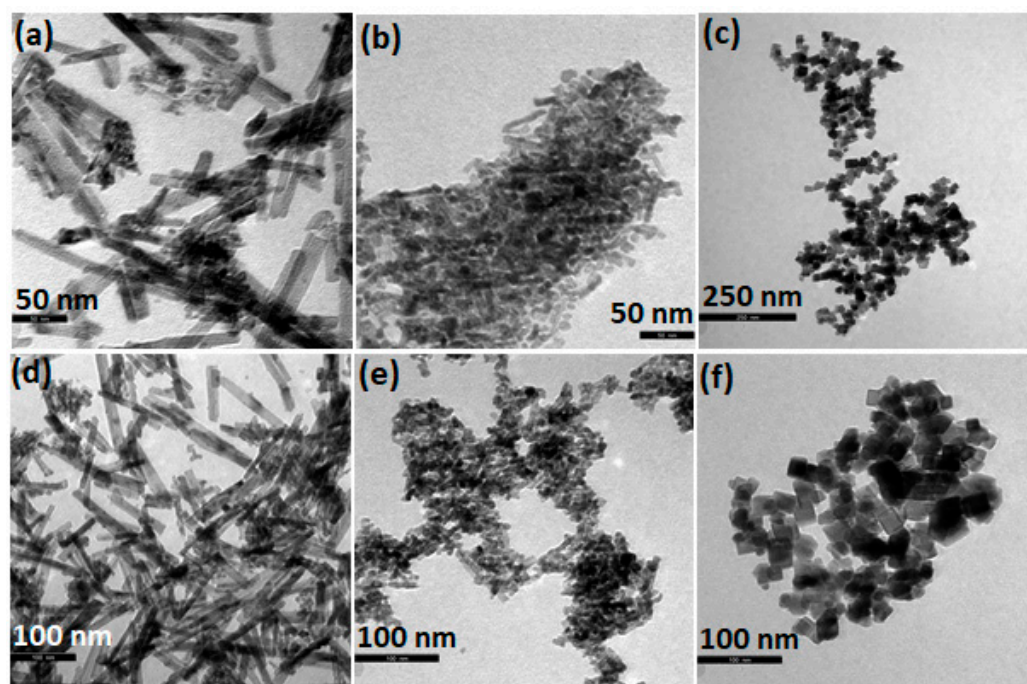


**Figure 3.** Indicative transmission electron microscopy (TEM) images of ceria (a,d) nanorods, (b,e) nanopolyhedra, and (c,f) nanocubes.

**Table 2.** Textural, structural and redox properties of bare ceria nanoparticles.

Sample	BET Analysis		XRD Analysis	TPR Analysis
	BET Surface Area (m <sup>2</sup> /g)	Pore Volume (cm <sup>3</sup> /g)	Average Crystallite Diameter, D <sub>XRD</sub> (nm) <sup>1</sup>	OSC (mmol O <sub>2</sub> /g) <sup>2</sup>
CeO <sub>2</sub> -NC	40	0.12	19.2	0.21
CeO <sub>2</sub> -NR	92	0.71	13.2	0.29
CeO <sub>2</sub> -NP	109	1.04	9.5	0.24

<sup>1</sup> Calculated applying Scherrer equation. <sup>2</sup> Calculated by integration of the temperature programmed reduction (TPR) peaks in the low-temperature range (surface oxygen reduction). OSC, oxygen storage capacity.

H<sub>2</sub>-TPR was performed to explore the impact of ceria shape on the redox properties (Figure 4). The main TPR peaks at ca. 550 and 800 °C are attributed to ceria's surface oxygen (O<sub>s</sub>) and bulk oxygen (O<sub>b</sub>) reduction, respectively. Interestingly, significant quantitative and qualitative differences between the reduction profiles are observed, implying the pivotal role of morphology on the redox features of ceria nanoparticles. In particular, the surface-to-bulk (O<sub>s</sub>/O<sub>b</sub>) ratio follows the order NR (1.13) > NP (0.94) > NC (0.71), which coincides with the oxygen storage capacity (OSC): NC (0.21 mmol/g) < NP (0.24 mmol/g) < NR (0.29 mmol/g). These results clearly showed that the rod-shaped ceria nanoparticles possess the highest population of weakly bound labile oxygen species. Moreover, ceria nanorods exhibit a low temperature reduction peak at 550 °C with a shoulder at ca. 450 °C, in opposition to other morphologies, which exhibit one main peak in the low temperature range. The latter is in agreement with the more facile reduction of {110} and {100} facets prevailing on ceria nanorods, as compared to {100} planes [76,112,114]. Hence, on the basis of the aforementioned results, it can be argued that, although ceria nanorods do not display the optimum textural properties (e.g., surface area), they possess the optimum redox characteristics in terms of population and facile reduction of loosely bound oxygen species, which is of paramount importance in several reaction processes obeying a redox mechanism, as further discussed below.

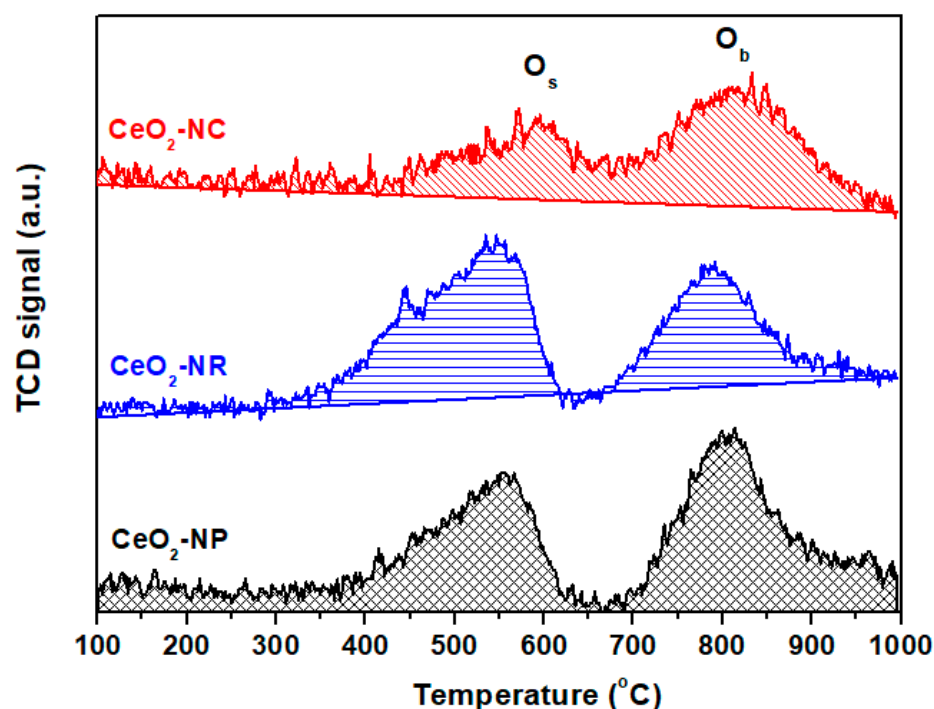
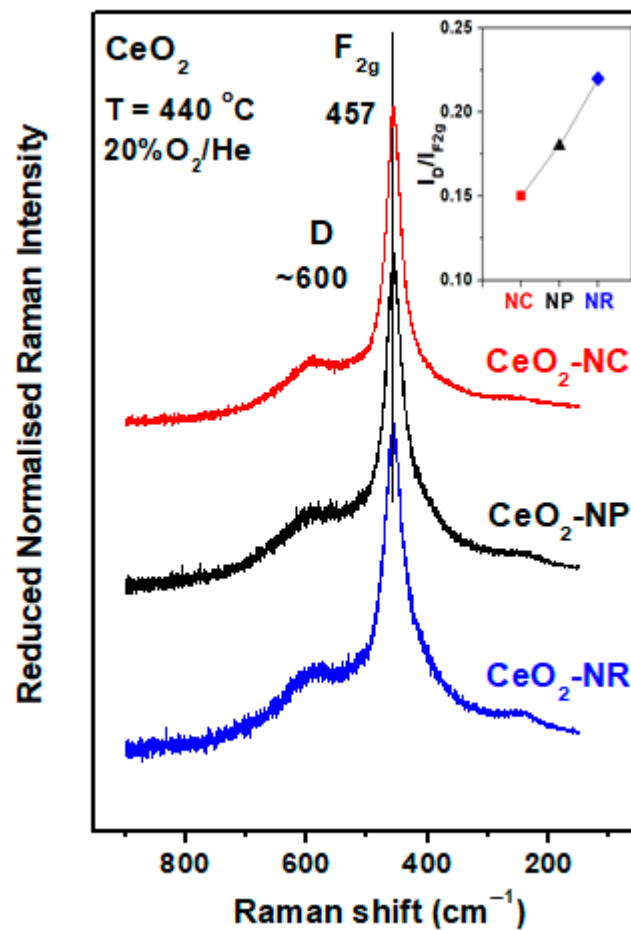


Figure 4. H<sub>2</sub>-TPR profiles of ceria nanoparticles.

More recently, the effect of ceria's exposed planes on the structural defects was more thoroughly investigated by in situ Raman spectroscopy, acquired under interchanging oxidized and reduced conditions [34]. Indicative results are depicted in Figure 5, where the in situ Raman spectra of bare ceria NR, NC and NP at 440 °C under oxidizing conditions are shown. The band at 457 cm<sup>-1</sup> is characteristic of F<sub>2g</sub> mode of Fm3m fluorite cubic structure, whereas the band D band at ca. 600 cm<sup>-1</sup> is ascribed to structural defects due to the perturbations in ceria lattice. Interestingly, the I<sub>D</sub>/I<sub>F2g</sub> ratio, which is a measure of lattice deformation and oxygen vacancies, follows the order NR > NP > NC in complete agreement with the reducibility order (*vide infra*). Hence, the relative population of structural defects and oxygen vacancies (Figure 5) coincides with ceria nanoparticle's reducibility (Figure 4 and Table 2), which is linked to Ce<sup>4+</sup> → Ce<sup>3+</sup> partial reduction and oxygen atoms detachment.

In addition, XPS analysis is performed to disclose the impact of ceria shape on elementary chemical states. Figure 6a demonstrates the Ce 3d XPS spectra of ceria nanoparticles, which can be deconvoluted into eight components [31,42,43,108,113,117–120]. In particular, the peaks at 900.7 eV (u), 907.6 eV (u'') and 916.4 eV (u''') correspond to the Ce 3d<sub>3/2</sub> spin-orbit components, while the peaks at 882.2 eV (v), 888.8 eV (v''), and 898.2 eV (v''') correspond to Ce 3d<sub>5/2</sub> spin-orbit components. These pairs of peaks are attributed to Ce<sup>4+</sup>, whereas the residual spectral lines at 902.1 eV (u') and 883.8 eV (v') are ascribed to Ce<sup>3+</sup> species. The Ce<sup>3+</sup>/Ce<sup>4+</sup> ratio is calculated by the corresponding peak's area and shown in Table 3. No significant differences were obtained among the samples of different morphology, varying between 0.32 and 0.33, in agreement with the relevant literature studies [107,121,122].



**Figure 5.** In situ Raman spectra for different ceria nanoshapes, i.e., NR, NP and NC. Inset depicts the  $I_D/I_{F_{2g}}$  intensity ratio. Laser power,  $w = 25$  mW; laser wavelength,  $\lambda_0 = 491.5$  nm; spectral slit width,  $6$   $\text{cm}^{-1}$ . Adapted from Reference [34]. Copyright© 2018, Elsevier.

**Table 3.** Surface properties of ceria nanoparticles.

Samples	XPS Analysis	
	$O_I/O_{II}$	$\text{Ce}^{3+}/\text{Ce}^{4+}$
CeO <sub>2</sub> -NC	1.99	0.33
CeO <sub>2</sub> -NP	2.04	0.32
CeO <sub>2</sub> -NR	2.13	0.33

The O 1s XPS spectra of ceria nanoparticles are presented in Figure 6b, exhibiting two characteristic peaks. The low binding energy (BE) peak ( $O_I$ ) at 529.4 eV corresponds to lattice oxygen, while the high BE peak ( $O_{II}$ ), at 531.3 eV is attributed to chemisorbed oxygen species, involving also hydroxyl groups, carbonate species, and adsorbed water. Interestingly, the  $O_I/O_{II}$  ratio (Table 3) follows the order NC (1.99) < NP (2.04) < NR (2.13), perfectly matched with the order of reducibility (Figure 4 and Table 2) and structural defects (Figure 5).

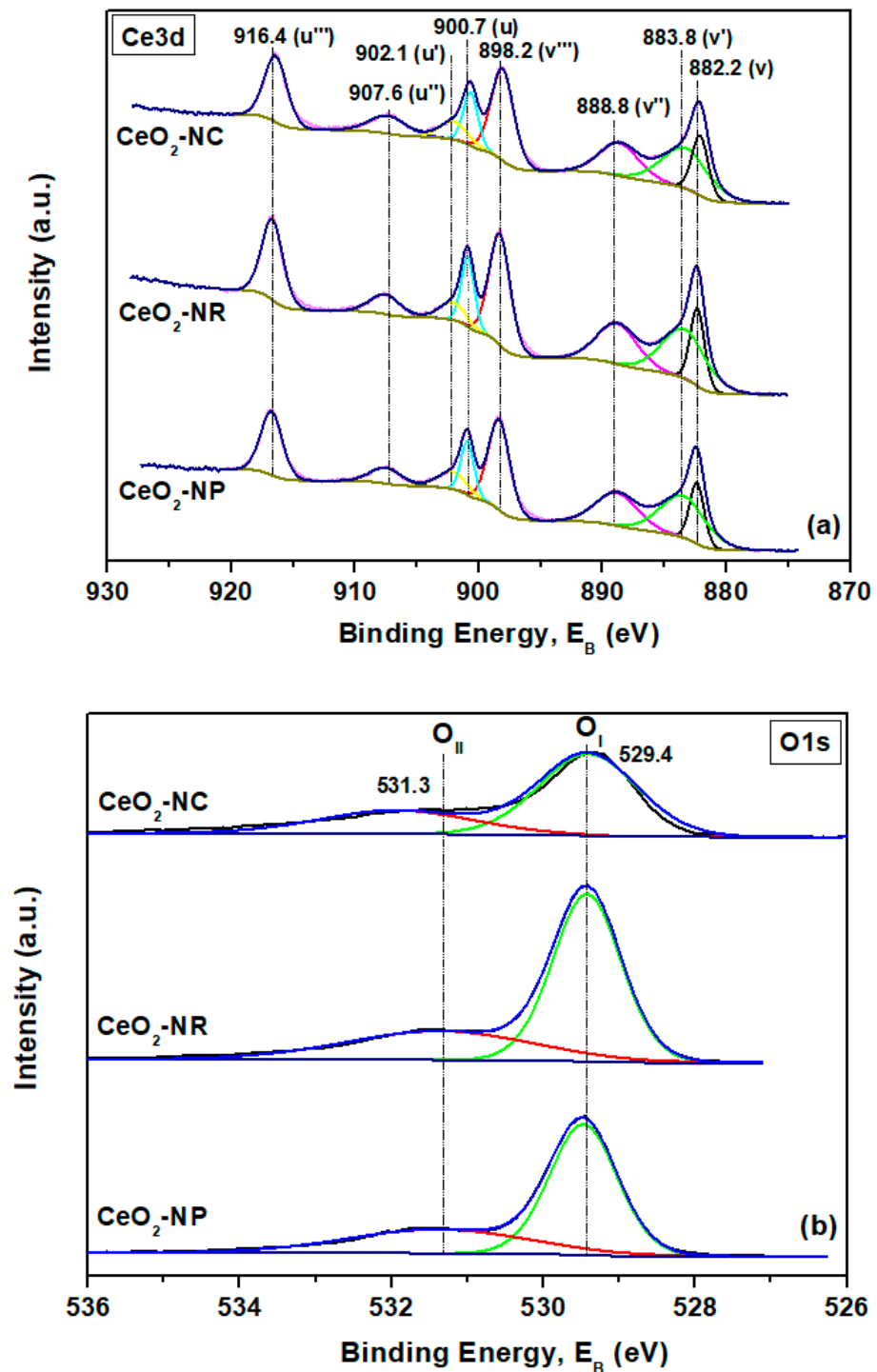


Figure 6. Ce 3d (a) and O 1s (b) XPS spectra of ceria nanoparticles.

#### 4. Physicochemical Properties of Ceria-Based Transition Metal (Fe, Co, Ni, and Cu) Catalysts

Having already established the pivotal role of ceria shape on the surface chemistry and redox properties of bare ceria nanoparticles, in this section, we discuss the combined effect of metal entity (Fe, Co, Ni, and Cu), ceria morphology and interfacial interactions on the physicochemical properties of TMs/CeO<sub>2</sub> oxides.

Figure 7 depicts representative TEM images of TMs (Fe, Co, Ni, and Cu)/CeO<sub>2</sub> samples. It is evident in all cases that ceria's morphology is not affected by the incorporation of transition metal to ceria, implying no morphological changes upon the addition of

TMs into the ceria carrier. The main textural, structural, and redox characteristics of all TMs/CeO<sub>2</sub> samples are summarized in Table 4.

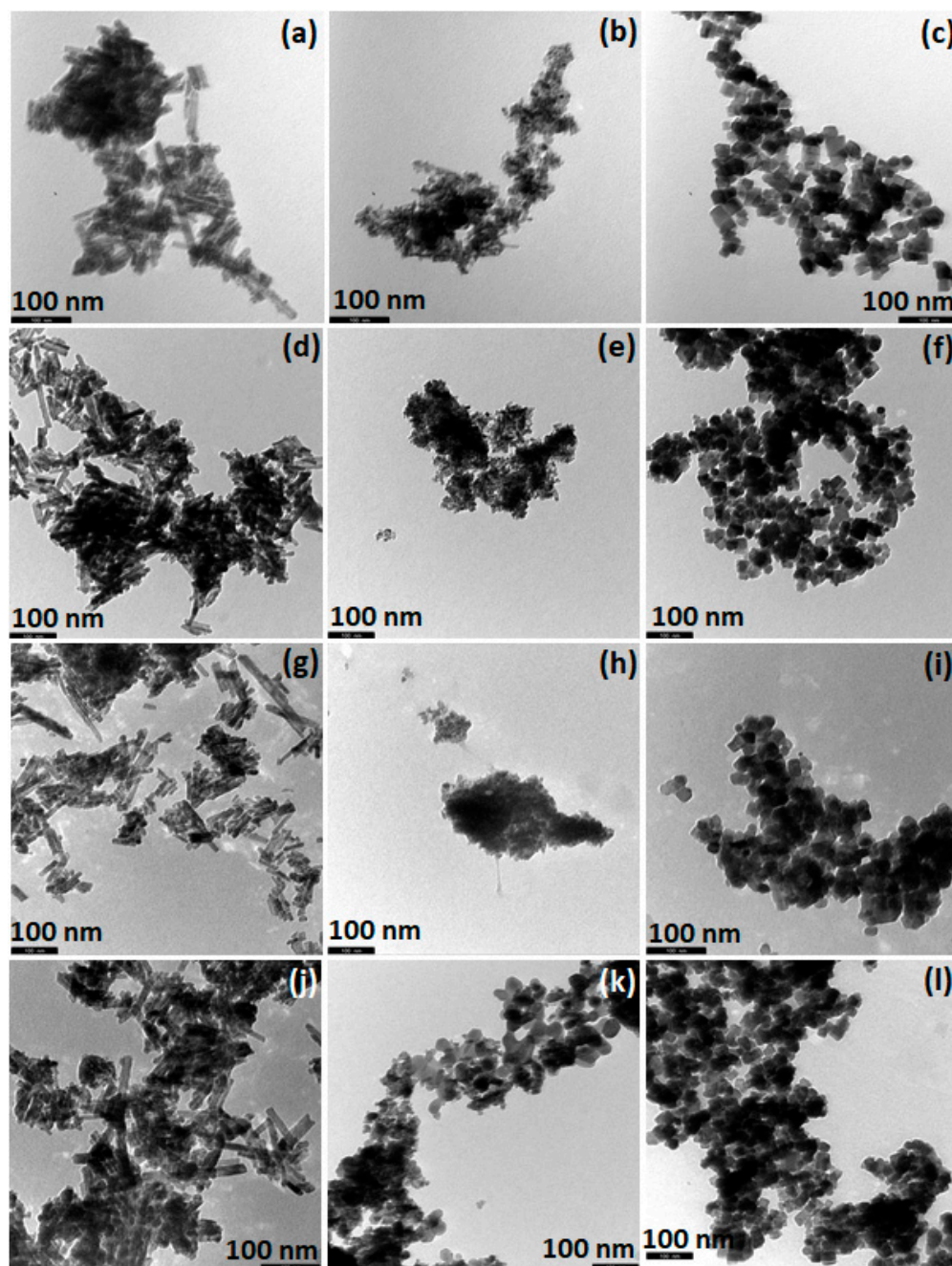


**Figure 7.** Indicative TEM images of TM/ceria (TM: Cu, Co, Fe, and Ni) nanoparticles: (a–c) Cu/CeO<sub>2</sub>, (d–f) Co/CeO<sub>2</sub>, (g–i) Fe/CeO<sub>2</sub>, and (j–l) Ni/CeO<sub>2</sub> samples of (a,d,g,j) rod-like, (b,e,h,k) polyhedral and (c,f,i,l) cubic morphology.

**Table 4.** Textural, structural and redox characteristics of ceria-supported transition metal catalysts.

Sample	BET Analysis		XRD Analysis		TPR Analysis
	BET Surface Area (m <sup>2</sup> /g)	Pore Volume (cm <sup>3</sup> /g)	Average Crystallite Diameter, D <sub>XRD</sub> (nm)		OSC (mmol O <sub>2</sub> /g)
			CeO <sub>2</sub>	CuO/Co <sub>3</sub> O <sub>4</sub> /Fe <sub>2</sub> O <sub>3</sub> /NiO	
Cu/CeO <sub>2</sub> -NC	34.3	0.29	19.2	52	0.75
Cu/CeO <sub>2</sub> -NR	75.4	0.40	11.6	43	0.90
Cu/CeO <sub>2</sub> -NP	90.7	0.29	9.6	31	0.83
Co/CeO <sub>2</sub> -NC	27.9	0.15	24	19	1.03
Co/CeO <sub>2</sub> -NR	71.8	0.31	14	16	1.19
Co/CeO <sub>2</sub> -NP	70.5	0.17	11	15	1.20
Fe/CeO <sub>2</sub> -NC	32.2	0.19	16.8	52.3	0.67
Fe/CeO <sub>2</sub> -NR	68.6	0.19	9.7	7.2	0.75
Fe/CeO <sub>2</sub> -NP	64.2	0.12	8.5	16.5	0.70
Ni/CeO <sub>2</sub> -NC	31.8	0.21	22	16.5	0.78
Ni/CeO <sub>2</sub> -NR	72.0	0.38	14	23	0.92
Ni/CeO <sub>2</sub> -NP	73.0	0.27	12	23	0.86

Concerning the BET area of bare ceria nanoparticles, the following order is obtained, as has been already discussed: NP > NR > NC (Table 2). The incorporation of transition metals into ceria support results in all cases into a slight decrease in surface area. In relation to the ceria crystallite size, it follows, generally, the reverse order of the BET area, i.e., the lower the surface area the larger the ceria crystallite size. In general, and on the basis of the present textural characteristics, it could be stated that the surface area and ceria crystallite size is not significantly affected by the transition metal's nature. The textural/structural properties of TMs/ceria catalysts are mainly determined by the support characteristics, as further corroborated by TEM analysis (Figure 7).

However, in complete contrast to textural/structural properties, the redox properties of TMs/ceria composites are notably affected upon metal incorporation to ceria carrier. In all cases, metal addition facilitates the surface oxygen reduction shifting the O<sub>s</sub> peak (Figure 4) to lower temperatures (not shown for brevity). In other words, the reduction of TMs/ceria composites is taking place at considerably lower temperatures in comparison to single metal and ceria oxides, indicating the beneficial impact of metal incorporation on surface oxygen reduction. In view of this fact, the metal–support interactions could be accounted for the enhanced reducibility and oxygen exchange kinetics of mixed oxides, as extensively discussed in previous studies [14,25,27,41,59,61]. The latter is further demonstrated by the estimation of OSC of TMs/CeO<sub>2</sub> catalysts in the low temperature region, in which the reduction of both the metal oxide (M<sub>x</sub>O<sub>y</sub>) and CeO<sub>2</sub> surface oxygen is taking place. The obtained OSC values (Table 4) always surpasses the theoretical values corresponding to nominal metal oxide (M<sub>x</sub>O<sub>y</sub>) content, revealing the metal-induced acceleration of ceria's capping oxygen reduction. More importantly, regardless of the metal entity (Cu, Co, Fe, and Ni), the OSC generally follows the order NR > NP > NC (Table 4), clearly demonstrating the crucial role of ceria nanostructure toward determining the redox properties of TMs/CeO<sub>2</sub> catalysts.

## 5. Implication in Catalysis

In this section the implications of shape engineering in catalysis are presented on the basis of ceria-based transition metals. In particular, the effect of ceria nanoparticles geometry on the catalytic behavior of TMs/CeO<sub>2</sub> oxides is demonstrated on the grounds of indicative oxidation/reduction reactions, such as CO oxidation, nitrous oxide (N<sub>2</sub>O) decomposition and CO<sub>2</sub> hydrogenation to value-added products. The main purpose of this section is to demonstrate the pivotal role of support morphology on catalysis based on our recent findings in the field [33–35,38,39,75], giving also particular emphasis to the establishment of reliable structure–performance relationships.

### 5.1. CO Oxidation

CO oxidation reaction has been widely studied in heterogeneous catalysis due to its involvement to various energy and environmental processes, such as the control of exhaust emissions from mobile and stationary sources, and fuel cell applications. Moreover, from the fundamental point of view, CO oxidation can be employed as a model reaction to disclose structure–performance relationships.

Ceria-based transition metal oxides have been extensively studied for CO oxidation, due mainly to their unique redox properties [2,3,9,56] and the peculiar metal–ceria synergistic interactions [16,41,123,124]. However, as previously mentioned, the distinct characteristics of both the active phase and ceria carrier (e.g., particle's size and shape) can exert a major impact on the redox properties, as well as the metal–support interactions, which can be consequently reflected on the catalytic activity. In this perspective, we recently explored the impact of ceria shape (nanocubes, nanorods, and nanopolyhedra) on the CO oxidation activity of various transition metals (e.g., Fe and Cu) supported on ceria nanoparticles. Herein, we summarize and discuss the main findings, which are interpreted based on the aforementioned characterization studies.

Figure 8 depicts the CO oxidation performance of the different bare ceria nanoshapes (NR, NC, and NP) in comparison to that of transition metal-based catalysts, i.e., Fe/CeO<sub>2</sub> and Cu/CeO<sub>2</sub> samples. Regarding, at first, the CO conversion of bare ceria, it is evident that significant differences are obtained between the samples, demonstrating the key role of morphology. On the basis of T<sub>50</sub>, i.e., the required temperature for 50% conversion, the following order is observed for bare ceria: NR (320 °C) < NP (350 °C) < NC (385 °C). It is noteworthy that the conversion order of bare ceria samples totally coincides with their relative concentration in labile oxygen species (expressed by OSC) and oxygen vacancies (expressed by the ratio of I<sub>D</sub>/I<sub>F2g</sub>). The latter clearly reveals the major role of ceria shape towards determining the redox/structural properties and in consequence the catalytic behavior, as further discussed below.

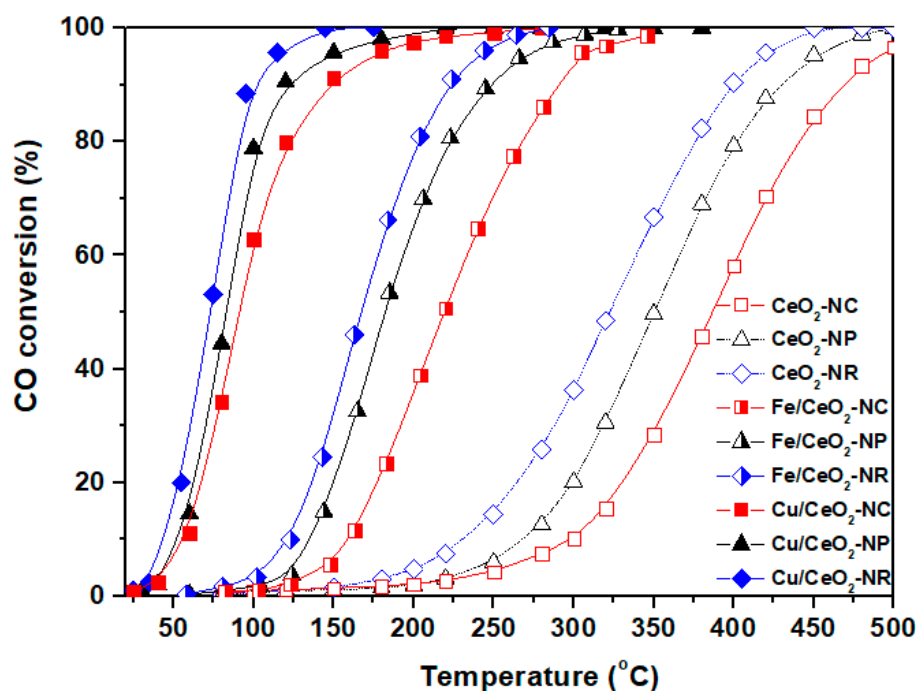


**Figure 8.** Ceria nanoparticles morphological effects (nanorods = NR, nanocubes = NC, nanopolyhedra = NP) on the CO oxidation performance of bare CeO<sub>2</sub>, Cu/CeO<sub>2</sub>, and Fe/CeO<sub>2</sub> samples.

Most significantly, the incorporation of transition metals (Fe and Cu) to ceria drastically improves the catalytic performance, not affecting, however, the activity order obtained for single CeO<sub>2</sub> samples. This clearly implies the guided role of support morphology on the

catalytic performance of ceria-based transition metal catalysts. Apparently, the rod-shaped samples exhibit the optimum catalytic efficiency, demonstrating complete CO conversion at 250 and 100 °C for Fe/CeO<sub>2</sub> and Cu/CeO<sub>2</sub> samples, respectively. It should be also mentioned that the optimum catalysts (Cu/CeO<sub>2</sub>-NR and Fe/CeO<sub>2</sub>-NR) attained a stable conversion performance in short-term stability tests (24 h). In view of this fact, BET and XRD analyses of the spent catalysts revealed no textural or structural modifications. In particular, ceria's mean crystallite size was slightly increased to 13 nm in comparison to 11.6 nm of the fresh sample, while the BET surface area remained practically unaltered (72.8 m<sup>2</sup>/g in comparison to 75.4 m<sup>2</sup>/g of the fresh sample, Table 4) [34,38].

The superior reactivity of samples with rod-like shape was further verified by a kinetic study, under differential reaction conditions, which revealed the following order in relation to apparent activation energy ( $E_a$ ): CeO<sub>2</sub>-NR (44.2 kJ/mol) < CeO<sub>2</sub>-NP (46.7 kJ/mol) < CeO<sub>2</sub>-NC (49.8 kJ/mol) [38]. A similar trend was acquired for TMs/ceria samples, indicating once again the pivotal role of ceria morphology towards determining the activity of ceria-based transition metal samples [38]. Moreover, the conversion performance of TMs/ceria samples prepared through the hydrothermal and consequent impregnation method surpasses, by far, the corresponding performance of mechanical mixtures (M<sub>x</sub>O<sub>y</sub> + CeO<sub>2</sub>-NR), clearly revealing the synergistic interactions between metal and support [38]. Finally, from a practical perspective, the catalytic performance of M<sub>x</sub>O<sub>y</sub>/CeO<sub>2</sub>-NR samples considerably surpasses the corresponding efficiency of typical precious metal oxidation catalysts, such as Pt/Al<sub>2</sub>O<sub>3</sub> (half-conversion temperature of ca. 230 °C under similar reaction conditions), revealing the effectiveness of shape engineering towards the rational design of cost-efficient noble metal-free catalysts [13].

The establishment of reliable structure–property relationships is crucial on the way to rational design and fabrication of highly–active composites. In other words, and in relation to the present findings, it is of paramount importance to disclose reliable correlations between key physicochemical parameters and the CO oxidation of M<sub>x</sub>O<sub>y</sub>/CeO<sub>2</sub> catalysts.

The aforementioned results can be well interpreted on the grounds of a Mars-van Krevelen mechanism, thoroughly described in our previous works [34,38,75]. Briefly, CO oxidation reaction proceeds through the following steps: (i) the chemisorption of CO on metal active sites followed by its migration to the metal–support interface, (ii) the activation of molecular oxygen to oxygen vacancies, (iii) the surface reaction between CO and active oxygen; and (iv) the replenishment of oxygen vacancies by gas phase oxygen. In view of this mechanistic scheme, the pivotal role of redox properties linked to oxygen vacancies and oxygen mobility is apparent. Indeed, perfect relationships between the reaction rate ( $r_{CO}$ , mmol s<sup>−1</sup> g<sup>−1</sup>) and the following activity descriptors were disclosed: (i) population of oxygen vacancies expressed by  $I_D/I_{F2g}$  ratio, and (ii) oxygen storage capacity (OSC), as shown in Figure 9. Similar relationships have been obtained for Cu- and Fe-based samples, revealing the pivotal role of support morphology [34,38].

Apparently, the CO consumption rate follows the order NR > NP > NC, which perfectly matched with the order of OSC and oxygen vacancies ( $I_D/I_{F2g}$ ). Hence, the improved OSC of nanorods with {100} and {110} exposed facets, linked with their abundance in oxygen vacancies, can be considered responsible for their enhanced CO oxidation performance. Correspondingly, both experimental and theoretical studies have revealed that the creation of anionic vacancies on ceria nanostructures is favored in the following order: {111} < {100} < {110} [22,24,65,112,125–132], which verifies the superiority of ceria nanorods during CO oxidation [105,133,134]. In a similar manner, it has been found that CO oxidation over CuO<sub>x</sub>/CeO<sub>2</sub> catalysts is sensitive to the structures of both copper and ceria, while the CuO<sub>x</sub>–ceria interaction depends on ceria's exposed facets, following the order: {110}-rods > {111}-polyhedra > {100}-cubes [135]. Similar effects have been reported for various noble metals (e.g., Au, Pd, and Pt) anchored on ceria nanorods during CO oxidation, water–gas shift (WGS) reaction, methanol steam reforming, etc. [68]; interfacial interactions in conjunction to the improved redox properties of ceria nanorods were mainly considered responsible for the enhanced catalytic efficiency [68].

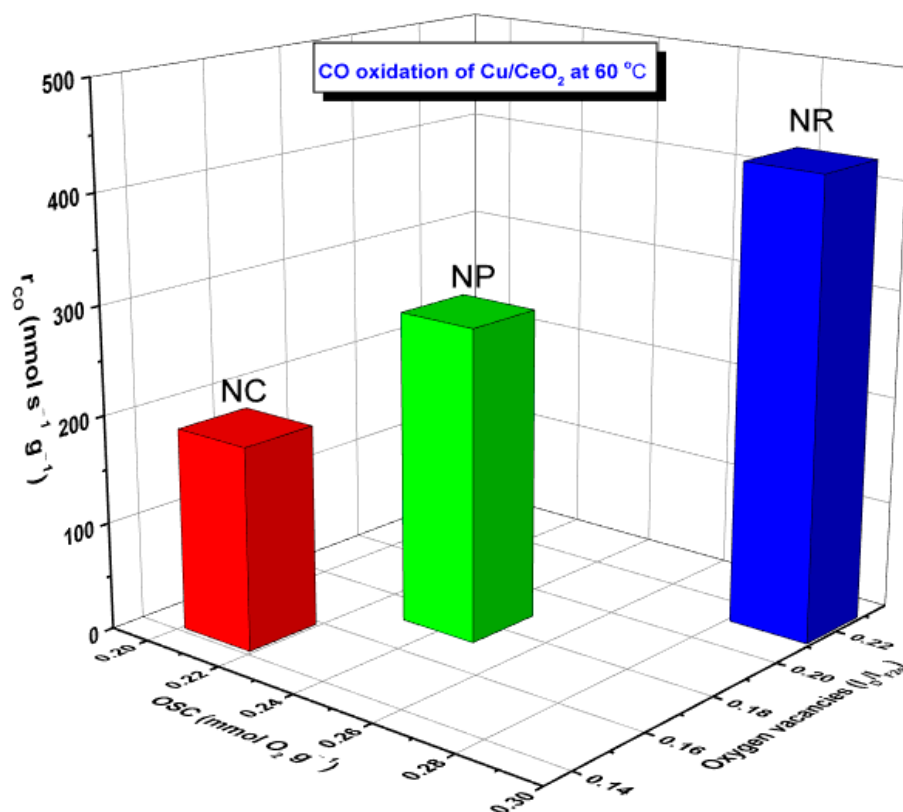


**Figure 9.** Relationship between the CO oxidation performance ( $r_{CO}$ , nmol s<sup>-1</sup> g<sup>-1</sup>) of Cu/CeO<sub>2</sub> samples and the oxygen storage capacity (OSC, mmol O<sub>2</sub> g<sup>-1</sup>) as well as the abundance of oxygen vacancies (in terms of I<sub>D</sub>/I<sub>F2g</sub> ratio) of ceria nanorods (NR), nanopolyhedra (NP) and nanocubes (NC).

## 5.2. N<sub>2</sub>O Decomposition

Nitrous oxide has been documented as a powerful greenhouse gas and ozone-depleting substance [136]. Noble metal-based catalysts are amongst the most efficient for the low-temperature deN<sub>2</sub>O process, being, however, highly expensive and sensitive to various off-gases in exhaust stream (e.g., O<sub>2</sub>). To this end, particular efforts have been lately devoted to the development of earth-abundant and highly-active NMs-free composites. The recent advances in the field of the rational design of NMs-free composites for N<sub>2</sub>O decomposition have been recently reviewed by our group [13,136]. It was revealed that the adjustment of local surface chemistry of earth-abundant metal oxides can lead to highly efficient catalyst formulations for real-life practical applications. Herein, in accordance to present article objectives, the ceria morphological effects on the deN<sub>2</sub>O process are presented on the basis of the latest advances in the field.

We recently explored the impact of ceria morphology (NR, NC, and NP) on the properties (*vide supra*) and the N<sub>2</sub>O decomposition behaviour of CoO<sub>x</sub>/CeO<sub>2</sub> samples. Figure 10 depicts the deN<sub>2</sub>O profiles of bare CeO<sub>2</sub> and Co/CeO<sub>2</sub> materials of various morphologies. As in the case of CO oxidation (Figure 8), the following order is observed for single ceria oxides: NR > NP > NC. Cobalt addition drastically improves the deN<sub>2</sub>O efficiency, not affecting, however, the conversion trend observed for ceria carriers, revealing the significant role of ceria nanostructure on the N<sub>2</sub>O decomposition over TMs/CeO<sub>2</sub> catalysts. It is also worth noticing that a similar trend was obtained under oxygen excess conditions (2.0 vol.%), whereas no loss in activity was observed in a short-term stability test (24 h) over the best catalyst (Co/CeO<sub>2</sub>-NR) [35].

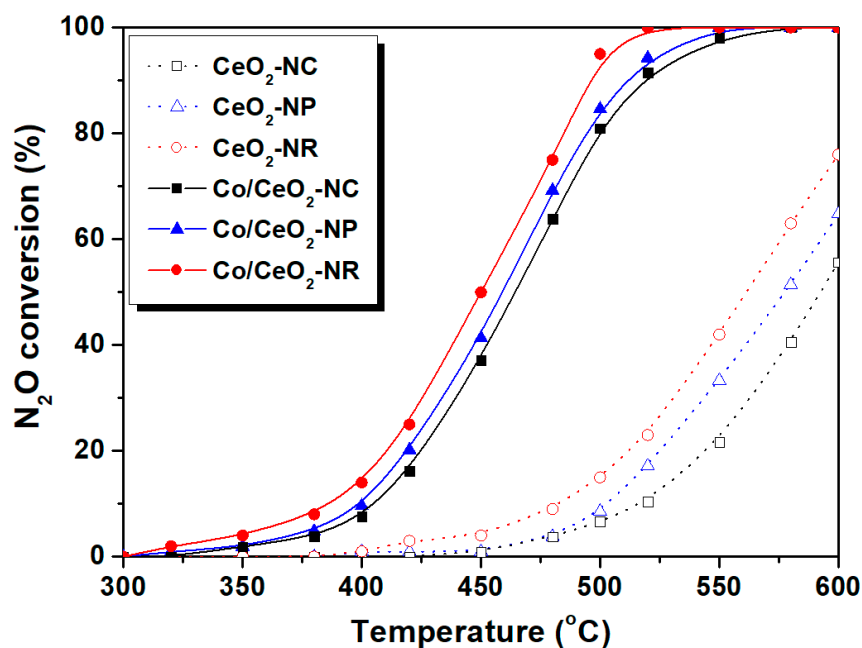


**Figure 10.** N<sub>2</sub>O conversion as a function of temperature for bare CeO<sub>2</sub> and Co/CeO<sub>2</sub> with nanorod (NR), nanopolyhedra (NP), and nanocubes (NC) morphology. Reaction conditions: 1000 ppm N<sub>2</sub>O, GHSV = 40,000 h<sup>-1</sup>.

The role of support morphology on the deN<sub>2</sub>O process could be corroborated on the ground of a redox-type mechanism, involving N<sub>2</sub>O dissociative adsorption on active cobalt sites followed by adsorbed oxygen species recombination towards the regeneration of active sites. The desorption of adsorbed oxygen either by recombining with neighboring oxygen atoms or by their interaction with N<sub>2</sub>O<sub>(ad)</sub> is considered as the rate-determining step (rds) [137]. In view of this mechanistic route, the redox properties of ceria and the cobalt–ceria interactions are considered to have a decisive role in the deN<sub>2</sub>O process. Indeed, a close correlation between the OSC of ceria nanoparticles and the deN<sub>2</sub>O activity was revealed (Figure 11), establishing reliable structure–activity relationships. CeO<sub>2</sub>-NR, followed by NP and NC, possesses the optimum oxygen storage capacity—linked to high population of oxygen vacancies and enhanced oxygen exchange kinetics—which is then reflected on the catalytic performance. Interestingly, the catalytic performance of Co/CeO<sub>2</sub> samples mirrors that of bare ceria samples, being however much superior. The latter clearly reveals that the morphology of the support in conjunction to metal addition can boost the catalytic performance, offering highly active deN<sub>2</sub>O catalysts [13,136].

Similarly, Liu et al. [114] revealed that the copper–ceria synergetic interactions can improve the reducibility and in turn the deN<sub>2</sub>O performance. In complete agreement, Pintar and co-workers [112] revealed the superior performance of copper clusters located on ceria nanorods in comparison to nanopolyhedra and nanocubes (Figure 12). According to a thorough characterization study, ceria nanorods facilitate the regeneration of active sites, due to their improved oxygen exchange kinetics, thus favoring the regeneration of active sites. The above mentioned results clearly demonstrate the effectiveness of shape engineering on the way to develop highly active deN<sub>2</sub>O catalysts.

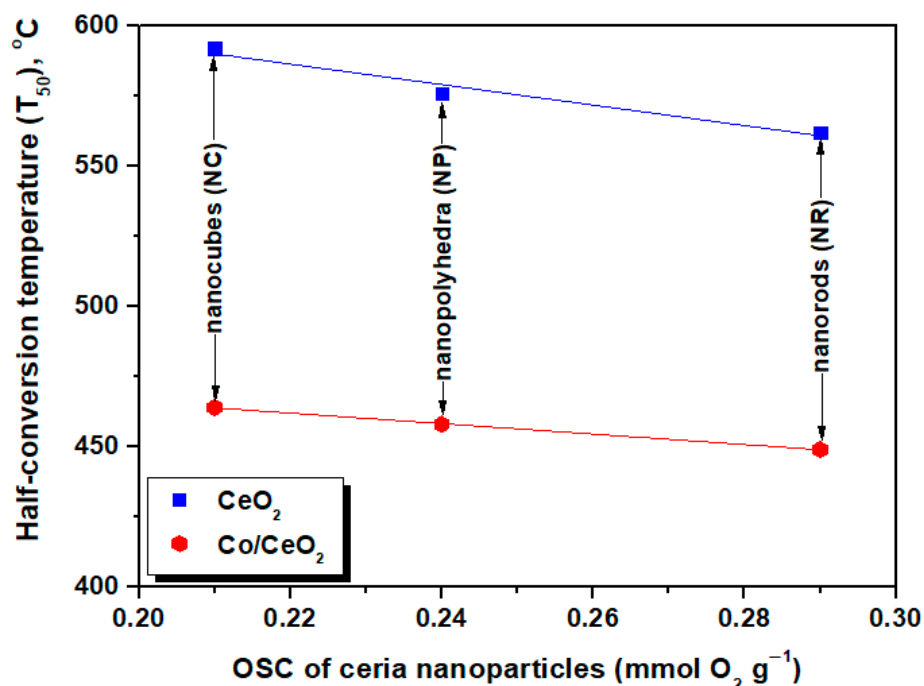


Figure 11. Relationship between the deN<sub>2</sub>O performance and the OSC (mmol O<sub>2</sub> g<sup>-1</sup>) of bare CeO<sub>2</sub> and Co/CeO<sub>2</sub> with nanorod (NR), nanopolyhedra (NP) and nanocubes (NC) morphology.

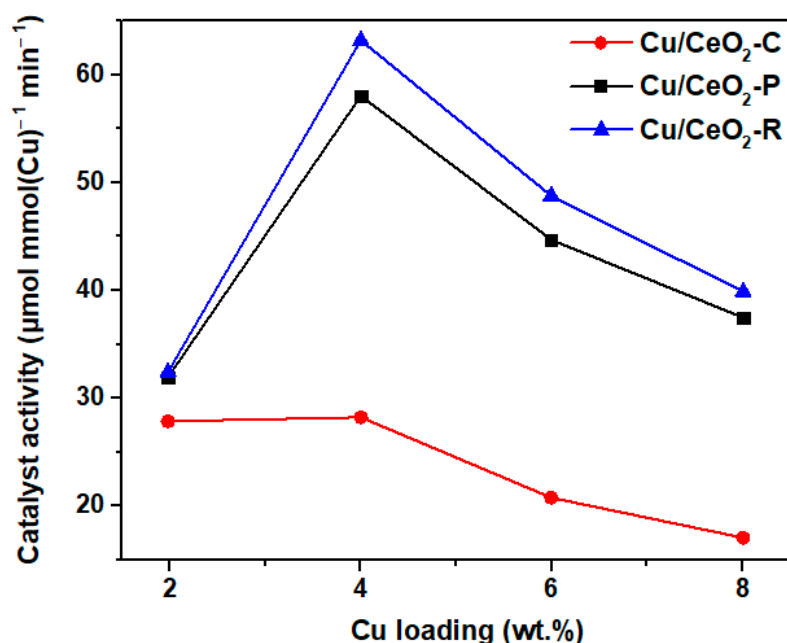
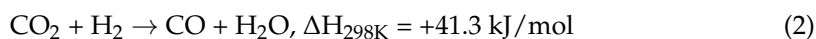
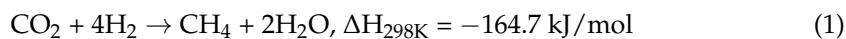


Figure 12. N<sub>2</sub>O decomposition rate of CuO<sub>x</sub>/CeO<sub>2</sub> samples of different morphology at 375 °C. Adapted from Reference [112]. Copyright© 2015, American Chemical Society.

### 5.3. CO<sub>2</sub> Hydrogenation

The unprecedented increase of CO<sub>2</sub> levels in the atmosphere due to anthropogenic activities related mainly to fossil fuels combustion has led to serious environmental consequences. Among the different mitigation approaches, carbon dioxide conversion to value-added products via its reaction with “green” hydrogen, has gained particular attention [138–141]. A plethora of chemical compounds, such as methane, carbon monoxide, methanol, and various hydrocarbons and oxygenates can be obtained through CO<sub>2</sub> hydrogenation [138,142,143]. This particular route can concurrently utilize CO<sub>2</sub> emissions

and the “green” hydrogen derived by the surplus power from non-intermittent Renewable Energy Sources (RES), providing, among others, CH<sub>4</sub> or CO through the reverse water–gas shift (rWGS) reaction (Equation (1)) and Sabatier reaction (Equation (2)), respectively:



Although noble metal catalytic materials, such as Rh and Ru, show satisfactory hydrogenation activity, their scarcity and high cost hinders widespread applications [144–147]. In this regard, our recent efforts have concentrated on the rational design of NMs-free catalyst formulations. Particular emphasis was given to middle–late 3d transition metals (e.g., Cu, Ni, Co, and Fe), due to their ability to chemisorb and consequently activate the CO<sub>2</sub> molecule [33,39]. Moreover, cerium oxide was selected as a supporting carrier due to its excellent redox/basic characteristics in conjunction to the synergistic interactions that can be developed between TMs and CeO<sub>2</sub>.

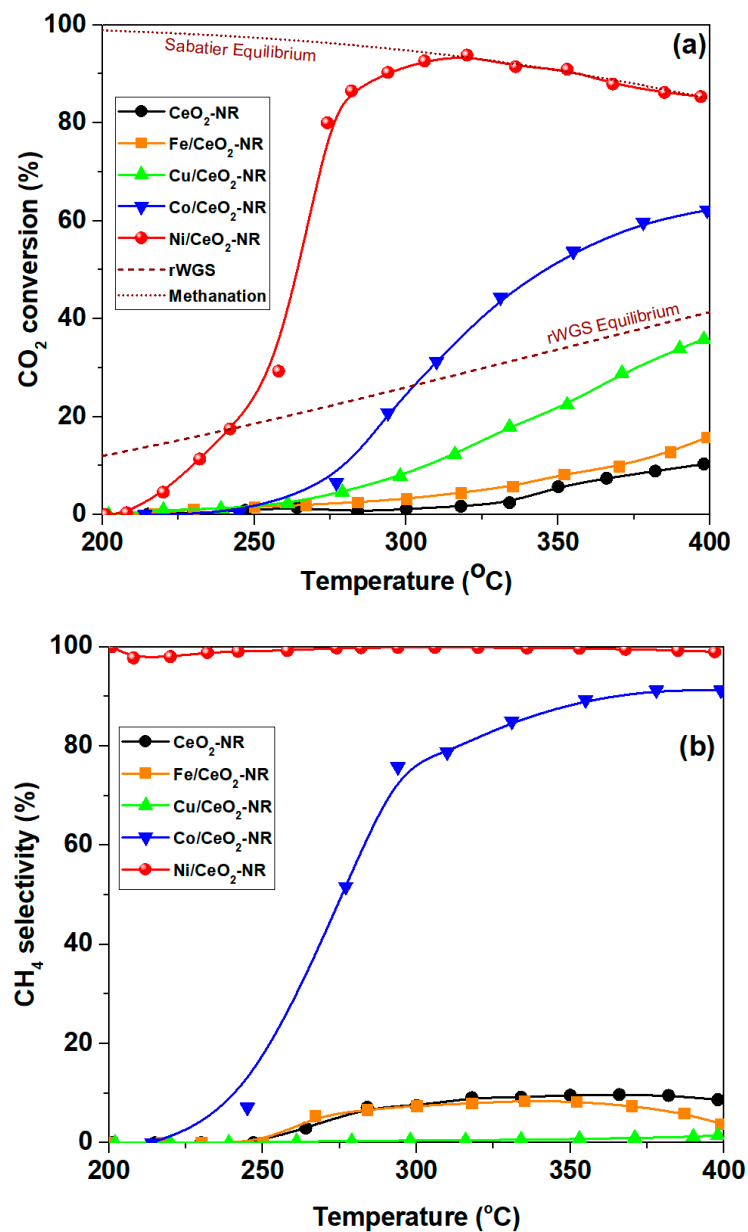
In line with the aforementioned fine-tuning aspects, ceria nanoparticles size/shape engineering at nanoscale could be of paramount importance. In view of this fact, and bearing in mind the crucial role of redox properties on CO<sub>2</sub> hydrogenation process [148], ceria nanoparticles of rod-like shape, offering the optimal redox properties, were selected as supporting carriers in order to obtain TMs/CeO<sub>2</sub>-NR composites.

Figure 13a,b demonstrates the conversion of CO<sub>2</sub> and the selectivity to methane, respectively, for bare CeO<sub>2</sub>-NR samples as well as for TMs (Fe, Co, Ni, and Cu)/CeO<sub>2</sub>-NR. It is obvious that there are significant differences between the samples, mostly depending on metal’s nature. Regarding CO<sub>2</sub> conversion, the following order is obtained: CeO<sub>2</sub> < Fe/CeO<sub>2</sub> < Cu/CeO<sub>2</sub> < Co/CeO<sub>2</sub> < Ni/CeO<sub>2</sub>, signifying the pivotal role of metal–support combination. Ni/CeO<sub>2</sub>-NR exhibits by far the optimum performance, offering ca. 92% conversion at 300 °C. In other words, by combining Ni with ceria nanorods extremely active CO<sub>2</sub> methanation catalysts can be obtained, which practically reach the equilibrium at very low temperatures of ca. 300 °C. More importantly, the high conversion performance of Ni catalysts is followed by 100% selectivity to CH<sub>4</sub> (Figure 13b) in the entire temperature range studied. Interestingly, the Cu/CeO<sub>2</sub>-NR catalyst is totally selective to CO (rWGS reaction), reaching the equilibrium at temperatures higher than 400 °C. Hence, the combination of Ni with CeO<sub>2</sub>-NR favors the CO<sub>2</sub> methanation reaction, whereas the rWGS reaction is favored over Cu/CeO<sub>2</sub>-NR. Moreover, stability experiments performed over the optimum catalytic materials (rod-shaped samples), revealed a stable performance without any deterioration of activity/selectivity [33,39].

The superior conversion and selectivity performance of Ni/CeO<sub>2</sub>-NR is additionally demonstrated by comparing it with the corresponding commercial ceria (CeO<sub>2</sub>-Com) and Ni/CeO<sub>2</sub>-Com of identical Ni/Ce atomic ratio (Ni/Ce = 0.25, corresponding to ca. 8 wt.% Ni loading; see Figure 14). Apparently, nickel–ceria nanorods are much superior as compared to the commercial ceria-supported sample (Ni/CeO<sub>2</sub>-Com), clearly revealing the major role of ceria support nanostructure. In particular, the Ni/CeO<sub>2</sub>-Com sample shows a CH<sub>4</sub> yield at 300 °C of ca. 7%, as compared to 92% for as-prepared Ni/CeO<sub>2</sub>-NR. These findings are of particular importance, revealing that by appropriately adjusting the composition (e.g., ceria with various TMs) and structural defects (e.g., by modulating ceria support morphology), highly active composites can be obtained.

In line with the aforementioned findings, significant morphological effects were also revealed during the CO<sub>2</sub> hydrogenation to CH<sub>3</sub>OH; the rod-shaped Cu/ceria samples have shown the highest methanol yield, ascribed mainly to the synergistic interactions between copper and ceria nanorods, as compared to nanocubes or nanoparticles [76]. Similarly, Cu/CeO<sub>2</sub>-NR shows the highest rWGS activity at atmospheric pressure as compared to nanospheres, since the formation of active intermediates is facilitated on the {110} facets of nanorods [84]. Moreover, among different morphologies (rods, cubes, octahedrons and polyhedrons), Pd supported on ceria nanorods has shown the highest activity and space–

time yield of methanol, due to their abundance in oxygen vacancies [149]. In this point, it should be mentioned that CO<sub>2</sub> hydrogenation catalysts of high activity and selectivity can be also obtained through the development of multicomponent systems [150,151]. For instance, highly active bimetallic composites supported on ceria nanoparticles (Cu-Ni/CeO<sub>2</sub>) of specific morphology (e.g., nanorods and nanotubes) can be obtained for the hydrogenation of carbon dioxide to methanol, due to the synergism between Cu-Ni alloy and ceria [150,151].



**Figure 13.** CO<sub>2</sub> conversion (a) and selectivity to CH<sub>4</sub> (b) for bare CeO<sub>2</sub>-NR and various metal-based catalysts (Fe, Cu, Co, Ni). Reaction conditions: Weight Hourly Space Velocity (WHSV) = 30,000 mL g<sup>-1</sup> h<sup>-1</sup>, H<sub>2</sub>:CO<sub>2</sub> = 4:1, P = 1 atm [39]. Dotted lines represent the corresponding equilibrium for rWGS and Sabatier reactions.

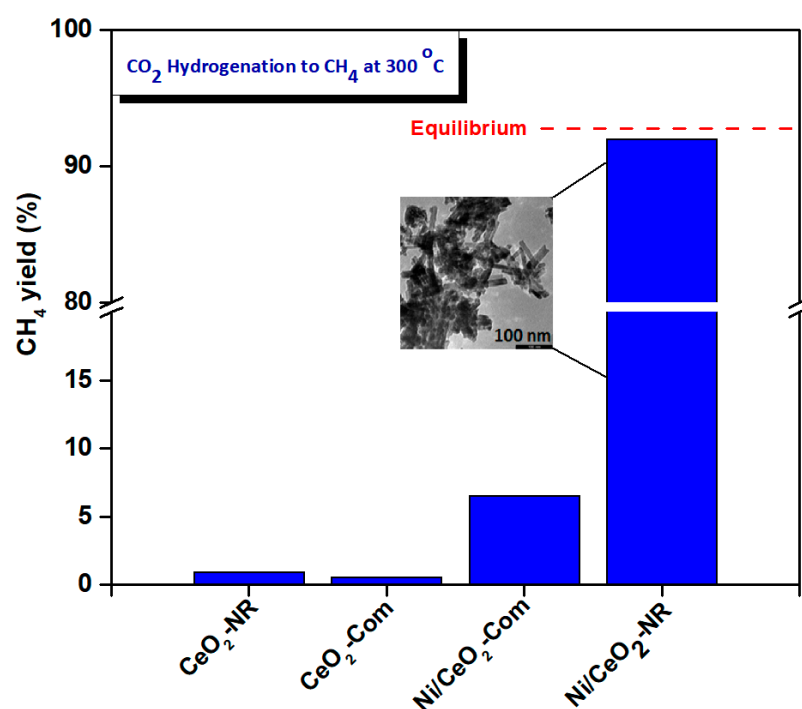


**Figure 14.** Methane Yield (defined as CO<sub>2</sub> conversion × selectivity to CH<sub>4</sub>) for CeO<sub>2</sub>-NR, commercial ceria (CeO<sub>2</sub>-Com) and the corresponding Ni-based samples. Reaction conditions: Weight Hourly Space Velocity = 30,000 mL g<sup>-1</sup> h<sup>-1</sup>, H<sub>2</sub>:CO<sub>2</sub> = 4:1, P = 1 atm [39].

At this point, driven by the aforementioned superior reactivity of ceria-based nanocomposites in various processes, it should be underlined that the development of structured catalysts, such as monoliths or pellets, coated with the catalytically active nanocomposites is a prerequisite for industrial applications. The materials platform for real-life industrial applications can be obtained by bringing together the following into one structure: the (i) superior catalytic activity of ceria-based nanocomposites of specific architecture; (ii) appropriate adhesion, pore structure, and permeability of washcoat; and (iii) enhanced thermal stability, mechanical strength, and low pressure drop of ceramic or metallic substrates [152–154].

## 6. Conclusions and Perspectives

In this review, we appraised the facet-dependent reactivity of ceria nanoparticles, on the ground of ceria-based transition metal catalysts. Through the morphological control of ceria nanoparticles (e.g., rods, cubes, and polyhedra), the concept of “shape engineering” can be employed to obtain reliable structure–performance relationships, which in turn could provide the basis for the rational design and fabrication of cost-efficient and highly-active catalyst formulations.

By means of a complementary characterization study, the morphological effects of ceria on key activity descriptors were initially explored. It was revealed that ceria nanoparticles with a rod shape possess excellent redox properties, related to their abundance in oxygen vacancies and weakly bound labile oxygen species. In particular, the following trend in relation to oxygen storage capacity (OSC) was obtained for bare ceria nanoparticles: rods > polyhedra > cubes, well correlated with the energy formation of anionic vacancies, i.e., {111} > {100} > {110}.

More importantly, it was clearly revealed that the incorporation of different transition metals (e.g., Cu, Fe, Ni, and Co) to ceria nanoparticles considerably accelerates surface oxygen reduction via metal–support interactions, following, however, the identical trend obtained for bare ceria nanoparticles. The latter clearly demonstrates the pivotal role of ceria morphology toward determining the redox features of ceria-based mixed oxides.

For reactions obeying a redox-type mechanism, where the redox cycle between labile and molecular oxygen mainly determines the reaction rate, perfect quantitative relationships between catalytic performance—redox properties—and ceria morphology were disclosed. From the practical perspective, extremely active composites were developed by concurrently adjusting the shape and composition of ceria-based mixed oxides. For instance, Cu/CeO<sub>2</sub>-nanorods exhibit full CO conversion at ca. 100 °C, surpassing by far the CO oxidation ability of a typical oxidation catalyst, such as Pt/Al<sub>2</sub>O<sub>3</sub>. In a similar manner, extremely active composites for CO<sub>2</sub> methanation were synthesized by combining Ni with CeO<sub>2</sub> nanorods.

Besides the alteration of solid state properties by the manipulation of shape at nanoscale, the fine adjustment of electronic state (e.g., by alkali promotion) can provide an additional powerful tool towards regulating the chemisorption properties and consequently the reactivity of metal oxides. Hence, the modulation of electronic state, size and shape at the nanoscale could provide the design direction on the way to fabricate cost-efficient earth-abundant metal-oxide catalysts for several environmental and energy processes. In this direction, the development of facile and versatile synthesis routes towards the precise control of shape and size at nanoscale is of paramount importance.

Moreover, the shape engineering of reducible carriers, such as ceria, could provide a powerful tool in order to rationally design and develop single atom supported catalysts with the anticipated activity and stability. The fine-tuning of the single metal atoms-support interaction through metal anchoring on specific crystal planes, could lead to interfacial sites of exceptional activity and stability.

Furthermore, it should be mentioned that the development of composite systems, through the combination of reducible oxide supports with bimetallic or carbide-based materials could lead to multifunctional composites with enhanced properties and catalytic performance.

Taking however into account the interrelated and multifaceted effects of shape, size, and electronic state on the reactivity of metal sites as well as on their interfacial interactions, especially under reaction conditions, it is of great difficulty to accurately discriminate the particular role of each adjusting parameter. In this context, complementary experimental studies (both in situ and ex situ), along with computational calculations and model studies are still required to unveil the underlying mechanism of catalytic phenomena.

Last but not least, the fabrication of highly-active ceria-based nanocomposites of specific architecture in the form of structured catalysts, such as honeycomb cordierite monoliths or pellets, could offer the scaffold for real-life energy and environmental industrial applications.

**Author Contributions:** M.L. contributed to paper writing; M.K. contributed to the conception, design and writing of the paper. All authors contributed to the discussion. All authors have read and agreed to the published version of the manuscript.

**Funding:** This research was co-financed by the European Union and Greek national funds through the Operational Program Competitiveness, Entrepreneurship and Innovation, under the call RESEARCH-CREATE-INNOVATE (project code: T1EDK-00094).

**Data Availability Statement:** The data presented in this review are from published sources.

**Conflicts of Interest:** The authors declare no conflict of interest.

## References

1. Yao, X.; Tang, C.; Gao, F.; Dong, L. Research progress on the catalytic elimination of atmospheric molecular contaminants over supported metal-oxide catalysts. *Catal. Sci. Technol.* **2014**, *4*, 2814–2829. [[CrossRef](#)]
2. Melchionna, M.; Fornasiero, P. The role of ceria-based nanostructured materials in energy applications. *Mater. Today* **2014**, *17*, 349–357. [[CrossRef](#)]
3. Montini, T.; Melchionna, M.; Monai, M.; Fornasiero, P. Fundamentals and Catalytic Applications of CeO<sub>2</sub>-Based Materials. *Chem. Rev.* **2016**, *116*, 5987–6041. [[CrossRef](#)]

4. Yuan, C.; Wu, H.B.; Xie, Y.; Lou, X.W. Mixed transition-metal oxides: Design, synthesis, and energy-related applications. *Angew. Chem. Int. Ed.* **2014**, *53*, 1488–1504. [[CrossRef](#)] [[PubMed](#)]
5. Su, X.; Yang, X.; Zhao, B.; Huang, Y. Designing of highly selective and high-temperature durable RWGS heterogeneous catalysts: Recent advances and the future directions. *J. Energy Chem.* **2017**, *26*, 854–867. [[CrossRef](#)]
6. Fang, Y.; Guo, Y. Copper-based non-precious metal heterogeneous catalysts for environmental remediation. *Chin. J. Catal.* **2018**, *39*, 566–582. [[CrossRef](#)]
7. Rodriguez, J.A.; Liu, P.; Graciani, J.; Senanayake, S.D.; Grinter, D.C.; Stacchiola, D.; Hrbek, J.; Fernández-Sanz, J. Inverse Oxide/Metal Catalysts in Fundamental Studies and Practical Applications: A Perspective of Recent Developments. *J. Phys. Chem. Lett.* **2016**, *7*, 2627–2639. [[CrossRef](#)]
8. Yang, W.; Wang, X.; Song, S.; Zhang, H. Syntheses and Applications of Noble-Metal-free CeO<sub>2</sub>-Based Mixed-Oxide Nanocatalysts. *Chem* **2019**, *5*, 1743–1774. [[CrossRef](#)]
9. Tang, W.-X.; Gao, P.-X. Nanostructured cerium oxide: Preparation, characterization, and application in energy and environmental catalysis. *MRS Commun.* **2016**, *6*, 311–329. [[CrossRef](#)]
10. Liu, L.; Corma, A. Metal Catalysts for Heterogeneous Catalysis: From Single Atoms to Nanoclusters and Nanoparticles. *Chem. Rev.* **2018**, *118*, 4981–5079. [[CrossRef](#)]
11. Zhuang, G.; Chen, Y.; Zhuang, Z.; Yu, Y.; Yu, J. Oxygen vacancies in metal oxides: Recent progress towards advanced catalyst design. *Sci. China Mater.* **2020**, *63*, 2089–2118. [[CrossRef](#)]
12. Zhou, Y.; Li, Y.; Shen, W. Shape Engineering of Oxide Nanoparticles for Heterogeneous Catalysis. *Chem. Asian J.* **2016**, *11*, 1470–1488. [[CrossRef](#)]
13. Konsolakis, M.; Lykaki, M. Recent advances on the rational design of non-precious metal oxide catalysts exemplified by CuO<sub>x</sub>/CeO<sub>2</sub> binary system: Implications of size, shape and electronic effects on intrinsic reactivity and metal-support interactions. *Catalysts* **2020**, *10*, 160. [[CrossRef](#)]
14. Hermes, E.D.; Jenness, G.R.; Schmidt, J.R. Decoupling the electronic, geometric and interfacial contributions to support effects in heterogeneous catalysis. *Mol. Simul.* **2015**, *41*, 123–133. [[CrossRef](#)]
15. Chen, Y.; Lai, Z.; Zhang, X.; Fan, Z.; He, Q.; Tan, C.; Zhang, H. Phase engineering of nanomaterials. *Nat. Rev. Chem.* **2020**, *4*, 243–256. [[CrossRef](#)]
16. Cargnello, M.; Doan-Nguyen, V.V.T.; Gordon, T.R.; Diaz, R.E.; Stach, E.A.; Gorte, R.J.; Fornasiero, P.; Murray, C.B. Control of metal nanocrystal size reveals metal-support interface role for ceria catalysts. *Science* **2013**, *341*, 771–773. [[CrossRef](#)] [[PubMed](#)]
17. Wang, H.; Lu, J. A Review on Particle Size Effect in Metal-Catalyzed Heterogeneous Reactions. *Chin. J. Chem.* **2020**, *38*, 1422–1444. [[CrossRef](#)]
18. Rudel, H.E.; Lane, M.K.M.; Muhich, C.L.; Zimmerman, J.B. Toward Informed Design of Nanomaterials: A Mechanistic Analysis of Structure-Property-Function Relationships for Faceted Nanoscale Metal Oxides. *ACS Nano* **2020**, *14*, 16472–16501. [[CrossRef](#)]
19. Sági, A.; Rajkumar, T.; Kiss, J.; Kukovecz, Á.; Kónya, Z.; Somorjai, G.A. Metallic Nanoparticles in Heterogeneous Catalysis. *Catal. Lett.* **2021**. [[CrossRef](#)]
20. Yang, F.; Deng, D.; Pan, X.; Fu, Q.; Bao, X. Understanding nano effects in catalysis. *Natl. Sci. Rev.* **2015**, *2*, 183–201. [[CrossRef](#)]
21. Wu, K.; Sun, L.-D.; Yan, C.-H. Recent Progress in Well-Controlled Synthesis of Ceria-Based Nanocatalysts towards Enhanced Catalytic Performance. *Adv. Energy Mater.* **2016**, *6*, 1600501. [[CrossRef](#)]
22. Trovarelli, A.; Llorca, J. Ceria Catalysts at Nanoscale: How Do Crystal Shapes Shape Catalysis? *ACS Catal.* **2017**, *7*, 4716–4735. [[CrossRef](#)]
23. Rodriguez, J.A.; Grinter, D.C.; Liu, Z.; Palomino, R.M.; Senanayake, S.D. Ceria-based model catalysts: Fundamental studies on the importance of the metal-ceria interface in CO oxidation, the water-gas shift, CO<sub>2</sub> hydrogenation, and methane and alcohol reforming. *Chem. Soc. Rev.* **2017**, *46*, 1824–1841. [[CrossRef](#)] [[PubMed](#)]
24. Qiao, Z.-A.; Wu, Z.; Dai, S. Shape-controlled ceria-based nanostructures for catalysis applications. *ChemSusChem* **2013**, *6*, 1821–1833. [[CrossRef](#)] [[PubMed](#)]
25. Puigdollers, A.R.; Schlexer, P.; Tosoni, S.; Pacchioni, G. Increasing oxide reducibility: The role of metal/oxide interfaces in the formation of oxygen vacancies. *ACS Catal.* **2017**, *7*, 6493–6513. [[CrossRef](#)]
26. Munnik, P.; De Jongh, P.E.; De Jong, K.P. Recent Developments in the Synthesis of Supported Catalysts. *Chem. Rev.* **2015**, *115*, 6687–6718. [[CrossRef](#)] [[PubMed](#)]
27. Mitchell, S.; Qin, R.; Zheng, N.; Pérez-Ramírez, J. Nanoscale engineering of catalytic materials for sustainable technologies. *Nat. Nanotechnol.* **2021**, *16*, 129–139. [[CrossRef](#)]
28. Konsolakis, M.; Sgourakis, M.; Carabineiro, S.A.C. Surface and redox properties of cobalt-ceria binary oxides: On the effect of Co content and pretreatment conditions. *Appl. Surf. Sci.* **2015**, *341*, 48–54. [[CrossRef](#)]
29. Kraia, T.; Kaklidis, N.; Konsolakis, M.; Marnellos, G.E. Hydrogen production by H<sub>2</sub>S decomposition over ceria supported transition metal (Co, Ni, Fe and Cu) catalysts. *Int. J. Hydrogen Energy* **2019**, *44*, 9753–9762. [[CrossRef](#)]
30. Carabineiro, S.A.C.; Chen, X.; Konsolakis, M.; Psarras, A.C.; Tavares, P.B.; Órfão, J.J.M.; Pereira, M.F.R.; Figueiredo, J.L. Catalytic oxidation of toluene on Ce-Co and La-Co mixed oxides synthesized by exotemplating and evaporation methods. *Catal. Today* **2015**, *244*, 161–171. [[CrossRef](#)]

31. Carabineiro, S.A.C.; Konsolakis, M.; Marnellos, G.E.N.; Asad, M.F.; Soares, O.S.G.P.; Tavares, P.B.; Pereira, M.F.R.; De Melo Órfão, J.J.; Figueiredo, J.L. Ethyl acetate abatement on copper catalysts supported on ceria doped with rare earth oxides. *Molecules* **2016**, *21*, 644. [[CrossRef](#)]
32. Díez-Ramírez, J.; Sánchez, P.; Kyriakou, V.; Zafeiratos, S.; Marnellos, G.E.; Konsolakis, M.; Dorado, F. Effect of support nature on the cobalt-catalyzed CO<sub>2</sub> hydrogenation. *J. CO<sub>2</sub> Util.* **2017**, *21*, 562–571. [[CrossRef](#)]
33. Konsolakis, M.; Lykaki, M.; Stefa, S.; Carabineiro, S.A.C.; Varvoutis, G.; Papista, E.; Marnellos, G.E. CO<sub>2</sub> Hydrogenation over Nanoceria-Supported Transition Metal Catalysts: Role of Ceria Morphology (Nanorods versus Nanocubes) and Active Phase Nature (Co versus Cu). *Nanomaterials* **2019**, *9*, 1739. [[CrossRef](#)]
34. Lykaki, M.; Pachatouridou, E.; Carabineiro, S.A.C.; Iliopoulou, E.; Andriopoulou, C.; Kallithrakas-Kontos, N.; Boghosian, S.; Konsolakis, M. Ceria nanoparticles shape effects on the structural defects and surface chemistry: Implications in CO oxidation by Cu/CeO<sub>2</sub> catalysts. *Appl. Catal. B Environ.* **2018**, *230*, 18–28. [[CrossRef](#)]
35. Lykaki, M.; Papista, E.; Kaklidis, N.; Carabineiro, S.A.C.; Konsolakis, M. Ceria Nanoparticles' Morphological Effects on the N<sub>2</sub>O Decomposition Performance of Co<sub>3</sub>O<sub>4</sub>/CeO<sub>2</sub> Mixed Oxides. *Catalysts* **2019**, *9*, 233. [[CrossRef](#)]
36. Stefa, S.; Lykaki, M.; Binas, V.; Pandis, P.K.; Stathopoulos, V.N.; Konsolakis, M. Hydrothermal Synthesis of ZnO-doped Ceria Nanorods: Effect of ZnO Content on the Redox Properties and the CO Oxidation Performance. *Appl. Sci.* **2020**, *10*, 7605. [[CrossRef](#)]
37. Stefa, S.; Lykaki, M.; Fragkoulis, D.; Binas, V.; Pandis, P.K.; Stathopoulos, V.N.; Konsolakis, M. Effect of the preparation method on the physicochemical properties and the CO oxidation performance of nanostructured CeO<sub>2</sub>/TiO<sub>2</sub> oxides. *Processes* **2020**, *8*, 847. [[CrossRef](#)]
38. Lykaki, M.; Stefa, S.; Pandis, P.K.; Stathopoulos, V.N.; Konsolakis, M. Facet-Dependent Reactivity of Fe<sub>2</sub>O<sub>3</sub>/CeO<sub>2</sub> Nanocomposites: Effect of Ceria Morphology on CO Oxidation. *Catalysts* **2019**, *9*, 371. [[CrossRef](#)]
39. Varvoutis, G.; Lykaki, M.; Stefa, S.; Papista, E.; Carabineiro, S.A.C.; Marnellos, G.E.; Konsolakis, M. Remarkable efficiency of Ni supported on hydrothermally synthesized CeO<sub>2</sub> nanorods for low-temperature CO<sub>2</sub> hydrogenation to methane. *Catal. Commun.* **2020**, *142*, 106036. [[CrossRef](#)]
40. Aneggi, E.; Boaro, M.; Colussi, S.; de Leitenburg, C.; Trovarelli, A. Chapter 289—Ceria-Based Materials in Catalysis: Historical Perspective and Future Trends. *Handb. Phys. Chem. Rare Earths* **2016**, *50*, 209–242. [[CrossRef](#)]
41. Konsolakis, M. The role of Copper–Ceria interactions in catalysis science: Recent theoretical and experimental advances. *Appl. Catal. B Environ.* **2016**, *198*, 49–66. [[CrossRef](#)]
42. Konsolakis, M.; Carabineiro, S.A.C.; Marnellos, G.E.; Asad, M.F.; Soares, O.S.G.P.; Pereira, M.F.R.; Órfão, J.J.M.; Figueiredo, J.L. Effect of cobalt loading on the solid state properties and ethyl acetate oxidation performance of cobalt-cerium mixed oxides. *J. Colloid Interface Sci.* **2017**, *496*, 141–149. [[CrossRef](#)]
43. Konsolakis, M.; Carabineiro, S.A.C.; Marnellos, G.E.; Asad, M.F.; Soares, O.S.G.P.; Pereira, M.F.R.; Órfão, J.J.M.; Figueiredo, J.L. Volatile organic compounds abatement over copper-based catalysts: Effect of support. *Inorg. Chim. Acta* **2017**, *455*, 473–482. [[CrossRef](#)]
44. Konsolakis, M.; Carabineiro, S.A.C.; Tavares, P.B.; Figueiredo, J.L. Redox properties and VOC oxidation activity of Cu catalysts supported on Ce<sub>1-x</sub>Sm<sub>x</sub>O<sub>8</sub> mixed oxides. *J. Hazard. Mater.* **2013**, *261*, 512–521. [[CrossRef](#)] [[PubMed](#)]
45. Konsolakis, M.; Ioakeimidis, Z. Surface/structure functionalization of copper-based catalysts by metal-support and/or metal-metal interactions. *Appl. Surf. Sci.* **2014**, *320*, 244–255. [[CrossRef](#)]
46. Konsolakis, M.; Ioakimidis, Z.; Kraia, T.; Marnellos, G.E. Hydrogen Production by Ethanol Steam Reforming (ESR) over CeO<sub>2</sub> Supported Transition Metal (Fe, Co, Ni, Cu) Catalysts: Insight into the Structure-Activity Relationship. *Catalysts* **2016**, *6*, 39. [[CrossRef](#)]
47. Zeng, S.; Zhang, W.; Guo, S.; Su, H. Inverse rod-like CeO<sub>2</sub> supported on CuO prepared by hydrothermal method for preferential oxidation of carbon monoxide. *Catal. Commun.* **2012**, *23*, 62–66. [[CrossRef](#)]
48. Rodriguez, J.A.; Liu, P.; Hrbek, J.; Evans, J.; Pérez, M. Water gas shift reaction on Cu and Au nanoparticles supported on CeO<sub>2</sub>(111) and ZnO(000 $\bar{1}$ ): Intrinsic activity and importance of support interactions. *Angew. Chem. Int. Ed.* **2007**, *46*, 1329–1332. [[CrossRef](#)]
49. Dong, L.; Yao, X.; Chen, Y. Interactions among supported copper-based catalyst components and their effects on performance: A review. *Chin. J. Catal.* **2013**, *34*, 851–864. [[CrossRef](#)]
50. Pacchioni, G. Electronic interactions and charge transfers of metal atoms and clusters on oxide surfaces. *Phys. Chem. Chem. Phys.* **2013**, *15*, 1737. [[CrossRef](#)]
51. Senanayake, S.D.; Rodriguez, J.A.; Stacchiola, D. Electronic metal-support interactions and the production of hydrogen through the water-gas shift reaction and ethanol steam reforming: Fundamental studies with well-defined model catalysts. *Top. Catal.* **2013**, *56*, 1488–1498. [[CrossRef](#)]
52. Capdevila-Cortada, M.; Vilé, G.; Teschner, D.; Pérez-Ramírez, J.; López, N. Reactivity descriptors for ceria in catalysis. *Appl. Catal. B Environ.* **2016**, *197*, 299–312. [[CrossRef](#)]
53. Mistry, H.; Behafarid, F.; Reske, R.; Varela, A.S.; Strasser, P.; Roldan Cuenya, B. Tuning Catalytic Selectivity at the Mesoscale via Interparticle Interactions. *ACS Catal.* **2016**, *6*, 1075–1080. [[CrossRef](#)]
54. Ahmadi, M.; Mistry, H.; Roldan Cuenya, B. Tailoring the Catalytic Properties of Metal Nanoparticles via Support Interactions. *J. Phys. Chem. Lett.* **2016**, *7*, 3519–3533. [[CrossRef](#)]
55. Beckers, J.; Rothenberg, G. Sustainable selective oxidations using ceria-based materials. *Green Chem.* **2010**, *12*, 939–948. [[CrossRef](#)]

56. Zhang, D.; Du, X.; Shi, L.; Gao, R. Shape-controlled synthesis and catalytic application of ceria nanomaterials. *Dalton Trans.* **2012**, *41*, 14455–14475. [[CrossRef](#)]
57. Sun, C.; Li, H.; Chen, L. Nanostructured ceria-based materials: Synthesis, properties, and applications. *Energy Environ. Sci.* **2012**, *5*, 8475–8505. [[CrossRef](#)]
58. Razmgar, K.; Altarawneh, M.; Oluwoye, I.; Senanayake, G. Ceria-Based Catalysts for Selective Hydrogenation Reactions: A Critical Review. *Catal. Surv. Asia* **2021**, *25*, 27–47. [[CrossRef](#)]
59. Van Deelen, T.W.; Hernández Mejía, C.; De Jong, K.P. Control of metal-support interactions in heterogeneous catalysts to enhance activity and selectivity. *Nat. Catal.* **2019**, *2*, 955–970. [[CrossRef](#)]
60. Di Sarli, V.; Landi, G.; Di Benedetto, A.; Lisi, L. Synergy Between Ceria and Metals (Ag or Cu) in Catalytic Diesel Particulate Filters: Effect of the Metal Content and of the Preparation Method on the Regeneration Performance. *Top. Catal.* **2021**, *64*, 256–269. [[CrossRef](#)]
61. Uzunoglu, A.; Zhang, H.; Andreescu, S.; Stanciu, L.A. CeO<sub>2</sub>–MO<sub>x</sub> (M: Zr, Ti, Cu) mixed metal oxides with enhanced oxygen storage capacity. *J. Mater. Sci.* **2015**, *50*, 3750–3762. [[CrossRef](#)]
62. Zhou, K.; Li, Y. Catalysis based on nanocrystals with well-defined facets. *Angew. Chem. Int. Ed.* **2012**, *51*, 602–613. [[CrossRef](#)]
63. Yuan, Q.; Duan, H.-H.; Li, L.-L.; Sun, L.-D.; Zhang, Y.-W.; Yan, C.-H. Controlled synthesis and assembly of ceria-based nanomaterials. *J. Colloid Interface Sci.* **2009**, *335*, 151–167. [[CrossRef](#)]
64. Xu, J.; Harmer, J.; Li, G.; Chapman, T.; Collier, P.; Longworth, S.; Tsang, S.C. Size dependent oxygen buffering capacity of ceria nanocrystals. *Chem. Commun.* **2010**, *46*, 1887–1889. [[CrossRef](#)] [[PubMed](#)]
65. Vilé, G.; Colussi, S.; Krumeich, F.; Trovarelli, A.; Pérez-Ramírez, J. Opposite face sensitivity of CeO<sub>2</sub> in hydrogenation and oxidation catalysis. *Angew. Chem. Int. Ed.* **2014**, *53*, 12069–12072. [[CrossRef](#)]
66. Ta, N.; Liu, J.; Shen, W. Tuning the shape of ceria nanomaterials for catalytic applications. *Chin. J. Catal.* **2013**, *34*, 838–850. [[CrossRef](#)]
67. Sayle, T.X.T.; Caddeo, F.; Zhang, X.; Sakthivel, T.; Das, S.; Seal, S.; Ptasinska, S.; Sayle, D.C. Structure-Activity Map of Ceria Nanoparticles, Nanocubes, and Mesoporous Architectures. *Chem. Mater.* **2016**, *28*, 7287–7295. [[CrossRef](#)]
68. Li, Y.; Shen, W. Morphology-dependent nanocatalysts: Rod-shaped oxides. *Chem. Soc. Rev.* **2014**, *43*, 1543–1574. [[CrossRef](#)]
69. Li, Y.; Liu, Q.; Shen, W. Morphology-dependent nanocatalysis: Metal particles. *Dalton Trans.* **2011**, *40*, 5811–5826. [[CrossRef](#)] [[PubMed](#)]
70. Dinh, C.T.; Nguyen, T.D.; Kleitz, F.; Do, T.O. Chapter 10–Shape-Controlled Synthesis of Metal Oxide Nanocrystals. In *Book Controlled Nanofabrication: Advances and Applications*, 1st ed.; Lui, R.-S., Ed.; Pan Stanford Publishing Pte. Ltd.: Singapore, 2012; pp. 327–367. ISBN 978-981-4316-87-3.
71. Datta, S.; Torrente-Murciano, L. Nanostructured faceted ceria as oxidation catalyst. *Curr. Opin. Chem. Eng.* **2018**, *20*, 99–106. [[CrossRef](#)]
72. Roldan Cuenya, B. Synthesis and catalytic properties of metal nanoparticles: Size, shape, support, composition, and oxidation state effects. *Thin Solid Film.* **2010**, *518*, 3127–3150. [[CrossRef](#)]
73. Cao, S.; Tao, F.F.; Tang, Y.; Li, Y.; Yu, J. Size- and shape-dependent catalytic performances of oxidation and reduction reactions on nanocatalysts. *Chem. Soc. Rev.* **2016**, *45*, 4747–4765. [[CrossRef](#)]
74. Aneggi, E.; Wiater, D.; De Leitenburg, C.; Llorca, J.; Trovarelli, A. Shape-dependent activity of ceria in soot combustion. *ACS Catal.* **2014**, *4*, 172–181. [[CrossRef](#)]
75. Lykaki, M.; Pachatouridou, E.; Iliopoulou, E.; Carabineiro, S.A.C.; Konsolakis, M. Impact of the synthesis parameters on the solid state properties and the CO oxidation performance of ceria nanoparticles. *RSC Adv.* **2017**, *7*, 6160–6169. [[CrossRef](#)]
76. Ouyang, B.; Tan, W.; Liu, B. Morphology effect of nanostructure ceria on the Cu/CeO<sub>2</sub> catalysts for synthesis of methanol from CO<sub>2</sub> hydrogenation. *Catal. Commun.* **2017**, *95*, 36–39. [[CrossRef](#)]
77. Zawadzki, M. Preparation and characterization of ceria nanoparticles by microwave-assisted solvothermal process. *J. Alloys Compd.* **2008**, *454*, 347–351. [[CrossRef](#)]
78. Zhang, Y.-W.; Si, R.; Liao, C.-S.; Yan, C.-H.; Xiao, C.-X.; Kou, Y. Facile alcohothermal synthesis, size-dependent ultraviolet absorption, and enhanced CO conversion activity of ceria nanocrystals. *J. Phys. Chem. B* **2003**, *107*, 10159–10167. [[CrossRef](#)]
79. Mai, H.-X.; Sun, L.-D.; Zhang, Y.-W.; Si, R.; Feng, W.; Zhang, H.-P.; Liu, H.-C.; Yan, C.-H. Shape-selective synthesis and oxygen storage behavior of ceria nanopolyhedra, nanorods, and nanocubes. *J. Phys. Chem. B* **2005**, *109*, 24380–24385. [[CrossRef](#)] [[PubMed](#)]
80. Gamarra, D.; Cámara, A.L.; Monte, M.; Rasmussen, S.B.; Chinchilla, L.E.; Hungría, A.B.; Munuera, G.; Gyorffy, N.; Schay, Z.; Cortés Corberán, V.; et al. Preferential oxidation of CO in excess H<sub>2</sub> over CuO/CeO<sub>2</sub> catalysts: Characterization and performance as a function of the exposed face present in the CeO<sub>2</sub> support. *Appl. Catal. B Environ.* **2013**, *130–131*, 224–238. [[CrossRef](#)]
81. Piumetti, M.; Bensaid, S.; Andana, T.; Dosa, M.; Novara, C.; Giorgis, F.; Russo, N.; Fino, D. Nanostructured Ceria-Based Materials: Effect of the Hydrothermal Synthesis Conditions on the Structural Properties and Catalytic Activity. *Catalysts* **2017**, *7*, 174. [[CrossRef](#)]
82. Araiza, D.G.; Gómez-Cortés, A.; Díaz, G. Partial oxidation of methanol over copper supported on nanoshaped ceria for hydrogen production. *Catal. Today* **2017**, *282*, 185–194. [[CrossRef](#)]
83. Yao, S.Y.; Xu, W.Q.; Johnston-Peck, A.C.; Zhao, F.Z.; Liu, Z.Y.; Luo, S.; Senanayake, S.D.; Martínez-Arias, A.; Liu, W.J.; Rodriguez, J.A. Morphological effects of the nanostructured ceria support on the activity and stability of CuO/CeO<sub>2</sub> catalysts for the water-gas shift reaction. *Phys. Chem. Chem. Phys.* **2014**, *16*, 17183–17195. [[CrossRef](#)] [[PubMed](#)]

84. Lin, L.; Yao, S.; Liu, Z.; Zhang, F.; Li, N.; Vovchok, D.; Martínez-Arias, A.; Castañeda, R.; Lin, J.; Senanayake, S.D.; et al. In Situ Characterization of Cu/CeO<sub>2</sub> Nanocatalysts for CO<sub>2</sub> Hydrogenation: Morphological Effects of Nanostructured Ceria on the Catalytic Activity. *J. Phys. Chem. C* **2018**, *122*, 12934–12943. [[CrossRef](#)]
85. Andana, T.; Piumetti, M.; Bensaid, S.; Veyre, L.; Thieuleux, C.; Russo, N.; Fino, D.; Quadrelli, E.A.; Pirone, R. CuO nanoparticles supported by ceria for NO<sub>x</sub>-assisted soot oxidation: Insight into catalytic activity and sintering. *Appl. Catal. B Environ.* **2017**, *216*, 41–58. [[CrossRef](#)]
86. Miceli, P.; Bensaid, S.; Russo, N.; Fino, D. Effect of the morphological and surface properties of CeO<sub>2</sub>-based catalysts on the soot oxidation activity. *Chem. Eng. J.* **2015**, *278*, 190–198. [[CrossRef](#)]
87. Gawade, P.; Mirkelamoglu, B.; Ozkan, U.S. The role of support morphology and impregnation medium on the water gas shift activity of ceria-supported copper catalysts. *J. Phys. Chem. C* **2010**, *114*, 18173–18181. [[CrossRef](#)]
88. Liu, J.; Li, Y.; Zhang, J.; He, D. Glycerol carbonylation with CO<sub>2</sub> to glycerol carbonate over CeO<sub>2</sub> catalyst and the influence of CeO<sub>2</sub> preparation methods and reaction parameters. *Appl. Catal. A Gen.* **2016**, *513*, 9–18. [[CrossRef](#)]
89. He, H.-W.; Wu, X.-Q.; Ren, W.; Shi, P.; Yao, X.; Song, Z.-T. Synthesis of crystalline cerium dioxide hydrosol by a sol-gel method. *Ceram. Int.* **2012**, *38* (Suppl. 1), S501–S504. [[CrossRef](#)]
90. Phonthammachai, N.; Rumruangwong, M.; Gulari, E.; Jamieson, A.M.; Jitkarnka, S.; Wongkasemjit, S. Synthesis and rheological properties of mesoporous nanocrystalline CeO<sub>2</sub> via sol-gel process. *Colloids Surf. A Physicochem. Eng. Asp.* **2004**, *247*, 61–68. [[CrossRef](#)]
91. Pinjari, D.V.; Pandit, A.B. Room temperature synthesis of crystalline CeO<sub>2</sub> nanopowder: Advantage of sonochemical method over conventional method. *Ultrason. Sonochem.* **2011**, *18*, 1118–1123. [[CrossRef](#)] [[PubMed](#)]
92. Yin, L.; Wang, Y.; Pang, G.; Koltypin, Y.; Gedanken, A. Sonochemical synthesis of cerium oxide nanoparticles—Effect of additives and quantum size effect. *J. Colloid Interface Sci.* **2002**, *246*, 78–84. [[CrossRef](#)] [[PubMed](#)]
93. Shang, H.; Zhang, X.; Xu, J.; Han, Y. Effects of preparation methods on the activity of CuO/CeO<sub>2</sub> catalysts for CO oxidation. *Front. Chem. Sci. Eng.* **2017**, *11*, 603–612. [[CrossRef](#)]
94. Zhou, L.; Li, X.; Yao, Z.; Chen, Z.; Hong, M.; Zhu, R.; Liang, Y.; Zhao, J. Transition-Metal Doped Ceria Microspheres with Nanoporous Structures for CO Oxidation. *Sci. Rep.* **2016**, *6*, 23900. [[CrossRef](#)] [[PubMed](#)]
95. Wang, W.-W.; Yu, W.-Z.; Du, P.-P.; Xu, H.; Jin, Z.; Si, R.; Ma, C.; Shi, S.; Jia, C.-J.; Yan, C.-H. Crystal Plane Effect of Ceria on Supported Copper Oxide Cluster Catalyst for CO Oxidation: Importance of Metal-Support Interaction. *ACS Catal.* **2017**, *7*, 1313–1329. [[CrossRef](#)]
96. Nakagawa, K.; Ohshima, T.; Tezuka, Y.; Katayama, M.; Katoh, M.; Sugiyama, S. Morphological effects of CeO<sub>2</sub> nanostructures for catalytic soot combustion of CuO/CeO<sub>2</sub>. *Catal. Today* **2015**, *246*, 67–71. [[CrossRef](#)]
97. Chaudhary, S.; Sharma, P.; Kumar, R.; Mehta, S.K. Nanoscale surface designing of Cerium oxide nanoparticles for controlling growth, stability, optical and thermal properties. *Ceram. Int.* **2015**, *41*, 10995–11003. [[CrossRef](#)]
98. Miyazaki, H.; Kato, J.I.; Sakamoto, N.; Wakiya, N.; Ota, T.; Suzuki, H. Synthesis of CeO<sub>2</sub> nanoparticles by rapid thermal decomposition using microwave heating. *Adv. Appl. Ceram.* **2010**, *109*, 123–127. [[CrossRef](#)]
99. Yang, H.; Huang, C.; Tang, A.; Zhang, X.; Yang, W. Microwave-assisted synthesis of ceria nanoparticles. *Mater. Res. Bull.* **2005**, *40*, 1690–1695. [[CrossRef](#)]
100. López, J.M.; Gilbank, A.L.; García, T.; Solsona, B.; Agouram, S.; Torrente-Murciano, L. The prevalence of surface oxygen vacancies over the mobility of bulk oxygen in nanostructured ceria for the total toluene oxidation. *Appl. Catal. B Environ.* **2015**, *174–175*, 403–412. [[CrossRef](#)]
101. Araiza, D.G.; Gómez-Cortés, A.; Díaz, G. Reactivity of methanol over copper supported on well-shaped CeO<sub>2</sub>: A TPD-DRIFTS study. *Catal. Sci. Technol.* **2017**, *7*, 5224–5235. [[CrossRef](#)]
102. Sudarsanam, P.; Hillary, B.; Amin, M.H.; Rockstroh, N.; Bentrup, U.; Brückner, A.; Bhargava, S.K. Heterostructured Copper-Ceria and Iron-Ceria Nanorods: Role of Morphology, Redox, and Acid Properties in Catalytic Diesel Soot Combustion. *Langmuir* **2018**, *34*, 2663–2673. [[CrossRef](#)]
103. Piumetti, M.; Bensaid, S.; Russo, N.; Fino, D. Nanostructured ceria-based catalysts for soot combustion: Investigations on the surface sensitivity. *Appl. Catal. B Environ.* **2015**, *165*, 742–751. [[CrossRef](#)]
104. Wang, S.; Zhao, L.; Wang, W.; Zhao, Y.; Zhang, G.; Ma, X.; Gong, J. Morphology control of ceria nanocrystals for catalytic conversion of CO<sub>2</sub> with methanol. *Nanoscale* **2013**, *5*, 5582–5588. [[CrossRef](#)] [[PubMed](#)]
105. Wu, Z.; Li, M.; Overbury, S.H. On the structure dependence of CO oxidation over CeO<sub>2</sub> nanocrystals with well-defined surface planes. *J. Catal.* **2012**, *285*, 61–73. [[CrossRef](#)]
106. Kovacevic, M.; Mojet, B.L.; Van Ommen, J.G.; Lefferts, L. Effects of Morphology of Cerium Oxide Catalysts for Reverse Water Gas Shift Reaction. *Catal. Lett.* **2016**, *146*, 770–777. [[CrossRef](#)]
107. Piumetti, M.; Andana, T.; Bensaid, S.; Russo, N.; Fino, D.; Pirone, R. Study on the CO Oxidation over Ceria-Based Nanocatalysts. *Nanoscale Res. Lett.* **2016**, *11*, 165. [[CrossRef](#)]
108. Guo, X.; Zhou, R. A new insight into the morphology effect of ceria on CuO/CeO<sub>2</sub> catalysts for CO selective oxidation in hydrogen-rich gas. *Catal. Sci. Technol.* **2016**, *6*, 3862–3871. [[CrossRef](#)]
109. Mock, S.A.; Sharp, S.E.; Stoner, T.R.; Radetic, M.J.; Zell, E.T.; Wang, R. CeO<sub>2</sub> nanorods-supported transition metal catalysts for CO oxidation. *J. Colloid Interface Sci.* **2016**, *466*, 261–267. [[CrossRef](#)]

110. Ren, Z.; Peng, F.; Li, J.; Liang, X.; Chen, B. Morphology-dependent properties of Cu/CeO<sub>2</sub> catalysts for the water-gas shift reaction. *Catalysts* **2017**, *7*, 48. [[CrossRef](#)]
111. He, H.; Yang, P.; Li, J.; Shi, R.; Chen, L.; Zhang, A.; Zhu, Y. Controllable synthesis, characterization, and CO oxidation activity of CeO<sub>2</sub> nanostructures with various morphologies. *Ceram. Int.* **2016**, *42*, 7810–7818. [[CrossRef](#)]
112. Zabilskiy, M.; Djinić, P.; Tchernychova, E.; Tkachenko, O.P.; Kustov, L.M.; Pintar, A. Nanoshaped CuO/CeO<sub>2</sub> Materials: Effect of the Exposed Ceria Surfaces on Catalytic Activity in N<sub>2</sub>O Decomposition Reaction. *ACS Catal.* **2015**, *5*, 5357–5365. [[CrossRef](#)]
113. Cui, Y.; Dai, W.-L. Support morphology and crystal plane effect of Cu/CeO<sub>2</sub> nanomaterial on the physicochemical and catalytic properties for carbonate hydrogenation. *Catal. Sci. Technol.* **2016**, *6*, 7752–7762. [[CrossRef](#)]
114. Liu, L.; Yao, Z.; Deng, Y.; Gao, F.; Liu, B.; Dong, L. Morphology and Crystal-Plane Effects of Nanoscale Ceria on the Activity of CuO/CeO<sub>2</sub> for NO Reduction by CO. *ChemCatChem* **2011**, *3*, 978–989. [[CrossRef](#)]
115. Xie, Y.; Wu, J.; Jing, G.; Zhang, H.; Zeng, S.; Tian, X.; Zou, X.; Wen, J.; Su, H.; Zhong, C.-J.; et al. Structural origin of high catalytic activity for preferential CO oxidation over CuO/CeO<sub>2</sub> nanocatalysts with different shapes. *Appl. Catal. B Environ.* **2018**, *239*, 665–676. [[CrossRef](#)]
116. Roldan Cuenya, B.; Beharid, F. Nanocatalysis: Size- and shape-dependent chemisorption and catalytic reactivity. *Surf. Sci. Rep.* **2015**, *70*, 135–187. [[CrossRef](#)]
117. Wang, C.; Cheng, Q.; Wang, X.; Ma, K.; Bai, X.; Tan, S.; Tian, Y.; Ding, T.; Zheng, L.; Zhang, J.; et al. Enhanced catalytic performance for CO preferential oxidation over CuO catalysts supported on highly defective CeO<sub>2</sub> nanocrystals. *Appl. Surf. Sci.* **2017**, *422*, 932–943. [[CrossRef](#)]
118. Wang, J.; Zhong, L.; Lu, J.; Chen, R.; Lei, Y.; Chen, K.; Han, C.; He, S.; Wan, G.; Luo, Y. A solvent-free method to rapidly synthesize CuO-CeO<sub>2</sub> catalysts to enhance their CO preferential oxidation: Effects of Cu loading and calcination temperature. *Mol. Catal.* **2017**, *443*, 241–252. [[CrossRef](#)]
119. Carabineiro, S.A.C.; Bastos, S.S.T.; Órfão, J.J.M.; Pereira, M.F.R.; Delgado, J.J.; Figueiredo, J.L. Exotemplated ceria catalysts with gold for CO oxidation. *Appl. Catal. A Gen.* **2010**, *381*, 150–160. [[CrossRef](#)]
120. Carabineiro, S.A.C.; Silva, A.M.T.; Dražić, G.; Tavares, P.B.; Figueiredo, J.L. Gold nanoparticles on ceria supports for the oxidation of carbon monoxide. *Catal. Today* **2010**, *154*, 21–30. [[CrossRef](#)]
121. Wu, Z.; Li, M.; Howe, J.; Meyer, H.M., III; Overbury, S.H. Probing defect sites on CeO<sub>2</sub> nanocrystals with well-defined surface planes by Raman spectroscopy and O<sub>2</sub> adsorption. *Langmuir* **2010**, *26*, 16595–16606. [[CrossRef](#)]
122. Solsona, B.; Sanchis, R.; Dejoz, A.M.; García, T.; Ruiz-Rodríguez, L.; López Nieto, J.M.; Cecilia, J.A.; Rodríguez-Castellón, E. Total Oxidation of Propane Using CeO<sub>2</sub> and CuO-CeO<sub>2</sub> Catalysts Prepared Using Templates of Different Nature. *Catalysts* **2017**, *7*, 96. [[CrossRef](#)]
123. Qiu, N.; Zhang, J.; Wu, Z. Peculiar surface-interface properties of nanocrystalline ceria-cobalt oxides with enhanced oxygen storage capacity. *Phys. Chem. Chem. Phys.* **2014**, *16*, 22659–22664. [[CrossRef](#)]
124. Konsolakis, M.; Carabineiro, S.A.C.; Papista, E.; Marnellos, G.E.; Tavares, P.B.; Agostinho Moreira, J.; Romaguera-Barcelay, Y.; Figueiredo, J.L. Effect of preparation method on the solid state properties and the deN<sub>2</sub>O performance of CuO-CeO<sub>2</sub> oxides. *Catal. Sci. Technol.* **2015**, *5*, 3714–3727. [[CrossRef](#)]
125. Sayle, T.X.T.; Parker, S.C.; Sayle, D.C. Oxidising CO to CO<sub>2</sub> using ceria nanoparticles. *Phys. Chem. Chem. Phys.* **2005**, *7*, 2936–2941. [[CrossRef](#)] [[PubMed](#)]
126. Sayle, T.X.T.; Cantoni, M.; Bhatta, U.M.; Parker, S.C.; Hall, S.R.; Möbus, G.; Molinari, M.; Reid, D.; Seal, S.; Sayle, D.C. Strain and architecture-tuned reactivity in ceria nanostructures; Enhanced catalytic oxidation of CO to CO<sub>2</sub>. *Chem. Mater.* **2012**, *24*, 1811–1821. [[CrossRef](#)]
127. Paier, J.; Penschke, C.; Sauer, J. Oxygen defects and surface chemistry of ceria: Quantum chemical studies compared to experiment. *Chem. Rev.* **2013**, *113*, 3949–3985. [[CrossRef](#)]
128. Li, Y.; Wei, Z.; Gao, F.; Kovarik, L.; Peden, C.H.F.; Wang, Y. Effects of CeO<sub>2</sub> support facets on VO<sub>x</sub>/CeO<sub>2</sub> catalysts in oxidative dehydrogenation of methanol. *J. Catal.* **2014**, *315*, 15–24. [[CrossRef](#)]
129. Mudiyansele, K.; Senanayake, S.D.; Feria, L.; Kundu, S.; Baber, A.E.; Graciani, J.; Vidal, A.B.; Agnoli, S.; Evans, J.; Chang, R.; et al. Importance of the metal-oxide interface in catalysis: In situ studies of the water-gas shift reaction by ambient-pressure X-ray photoelectron spectroscopy. *Angew. Chem. Int. Ed.* **2013**, *52*, 5101–5105. [[CrossRef](#)] [[PubMed](#)]
130. Mayernick, A.D.; Janik, M.J. Methane activation and oxygen vacancy formation over CeO<sub>2</sub> and Zr, Pd substituted CeO<sub>2</sub> surfaces. *J. Phys. Chem. C* **2008**, *112*, 14955–14964. [[CrossRef](#)]
131. Nolan, M.; Grigoleit, S.; Sayle, D.C.; Parker, S.C.; Watson, G.W. Density functional theory studies of the structure and electronic structure of pure and defective low index surfaces of ceria. *Surf. Sci.* **2005**, *576*, 217–229. [[CrossRef](#)]
132. Nolan, M.; Parker, S.C.; Watson, G.W. The electronic structure of oxygen vacancy defects at the low index surfaces of ceria. *Surf. Sci.* **2005**, *595*, 223–232. [[CrossRef](#)]
133. Zhou, K.; Xu, R.; Sun, X.; Chen, H.; Tian, Q.; Shen, D.; Li, Y. Favorable synergetic effects between CuO and the reactive planes of ceria nanorods. *Catal. Lett.* **2005**, *101*, 169–173. [[CrossRef](#)]
134. Dong, F.; Meng, Y.; Han, W.; Zhao, H.; Tang, Z. Morphology effects on surface chemical properties and lattice defects of Cu/CeO<sub>2</sub> catalysts applied for low-temperature CO oxidation. *Sci. Rep.* **2019**, *9*, 12056. [[CrossRef](#)]
135. Gao, Y.; Zhang, Z.; Li, Z.; Huang, W. Understanding morphology-dependent CuO<sub>x</sub>-CeO<sub>2</sub> interactions from the very beginning. *Chin. J. Catal.* **2020**, *41*, 1006–1016. [[CrossRef](#)]

136. Konsolakis, M. Recent Advances on Nitrous Oxide (N<sub>2</sub>O) Decomposition over Non-Noble-Metal Oxide Catalysts: Catalytic Performance, Mechanistic Considerations, and Surface Chemistry Aspects. *ACS Catal.* **2015**, *5*, 6397–6421. [[CrossRef](#)]
137. Wu, L.; Qin, W.; Hu, X.; Ju, S.; Dong, C.; Yang, Y. Decomposition and reduction of N<sub>2</sub>O on CaS (100) surface: A theoretical account. *Surf. Sci.* **2015**, *632*, 83–87. [[CrossRef](#)]
138. Atsbha, T.A.; Yoon, T.; Seongho, P.; Lee, C.-J. A review on the catalytic conversion of CO<sub>2</sub> using H<sub>2</sub> for synthesis of CO, methanol, and hydrocarbons. *J. CO<sub>2</sub> Util.* **2021**, *44*, 101413. [[CrossRef](#)]
139. Hoekman, S.K.; Broch, A.; Robbins, C.; Purcell, R. CO<sub>2</sub> recycling by reaction with renewably-generated hydrogen. *Int. J. Greenh. Gas Control* **2010**, *4*, 44–50. [[CrossRef](#)]
140. Yang, N.; Wang, R. Sustainable technologies for the reclamation of greenhouse gas CO<sub>2</sub>. *J. Clean. Prod.* **2015**, *103*, 784–792. [[CrossRef](#)]
141. Hepburn, C.; Adlen, E.; Beddington, J.; Carter, E.A.; Fuss, S.; Mac Dowell, N.; Minx, J.C.; Smith, P.; Williams, C.K. The technological and economic prospects for CO<sub>2</sub> utilization and removal. *Nature* **2019**, *575*, 87–97. [[CrossRef](#)]
142. Rafiee, A.; Rajab Khalilpour, K.; Milani, D.; Panahi, M. Trends in CO<sub>2</sub> conversion and utilization: A review from process systems perspective. *J. Environ. Chem. Eng.* **2018**, *6*, 5771–5794. [[CrossRef](#)]
143. Kamkeng, A.D.N.; Wang, M.; Hu, J.; Du, W.; Qian, F. Transformation technologies for CO<sub>2</sub> utilisation: Current status, challenges and future prospects. *Chem. Eng. J.* **2021**, *409*, 128138. [[CrossRef](#)]
144. Kacimi, S.; Barbier, J., Jr.; Taha, R.; Duprez, D. Oxygen storage capacity of promoted Rh/CeO<sub>2</sub> catalysts. Exceptional behavior of RhCu/CeO<sub>2</sub>. *Catal. Lett.* **1993**, *22*, 343–350. [[CrossRef](#)]
145. Tada, S.; Ochieng, O.J.; Kikuchi, R.; Haneda, T.; Kameyama, H. Promotion of CO<sub>2</sub> methanation activity and CH<sub>4</sub> selectivity at low temperatures over Ru/CeO<sub>2</sub>/Al<sub>2</sub>O<sub>3</sub> catalysts. *Int. J. Hydrogen Energy* **2014**, *39*, 10090–10100. [[CrossRef](#)]
146. Martin, N.M.; Velin, P.; Skoglundh, M.; Bauer, M.; Carlsson, P.-A. Catalytic hydrogenation of CO<sub>2</sub> to methane over supported Pd, Rh and Ni catalysts. *Catal. Sci. Technol.* **2017**, *7*, 1086–1094. [[CrossRef](#)]
147. Karelovic, A.; Ruiz, P. CO<sub>2</sub> hydrogenation at low temperature over Rh/ $\gamma$ -Al<sub>2</sub>O<sub>3</sub> catalysts: Effect of the metal particle size on catalytic performances and reaction mechanism. *Appl. Catal. B Environ.* **2012**, *113–114*, 237–249. [[CrossRef](#)]
148. Dreyer, J.A.H.; Li, P.; Zhang, L.; Beh, G.K.; Zhang, R.; Sit, P.H.-L.; Teoh, W.Y. Influence of the oxide support reducibility on the CO<sub>2</sub> methanation over Ru-based catalysts. *Appl. Catal. B Environ.* **2017**, *219*, 715–726. [[CrossRef](#)]
149. Jiang, F.; Wang, S.; Liu, B.; Liu, J.; Wang, L.; Xiao, Y.; Xu, Y.; Liu, X. Insights into the Influence of CeO<sub>2</sub> Crystal Facet on CO<sub>2</sub> Hydrogenation to Methanol over Pd/CeO<sub>2</sub> Catalysts. *ACS Catal.* **2020**, *10*, 11493–11509. [[CrossRef](#)]
150. Tan, Q.; Shi, Z.; Wu, D. CO<sub>2</sub> hydrogenation over differently morphological CeO<sub>2</sub>-supported Cu-Ni catalysts. *Int. J. Energy Res.* **2019**, *43*, 5392–5404. [[CrossRef](#)]
151. Tan, Q.; Shi, Z.; Wu, D. CO<sub>2</sub> Hydrogenation to Methanol over a Highly Active Cu-Ni/CeO<sub>2</sub>-Nanotube Catalyst. *Ind. Eng. Chem. Res.* **2018**, *57*, 10148–10158. [[CrossRef](#)]
152. Pérez, V.R.; Bueno-López, A. Catalytic regeneration of Diesel Particulate Filters: Comparison of Pt and CePr active phases. *Chem. Eng. J.* **2015**, *279*, 79–85. [[CrossRef](#)]
153. Di Sarli, V.; Landi, G.; Lisi, L.; Saliva, A.; Di Benedetto, A. Catalytic diesel particulate filters with highly dispersed ceria: Effect of the soot-catalyst contact on the regeneration performance. *Appl. Catal. B Environ.* **2016**, *197*, 116–124. [[CrossRef](#)]
154. Lv, C.; Chen, H.; Hu, M.; Ai, T.; Fu, H. Nano-oxides washcoat for enhanced catalytic oxidation activity toward the perovskite-based monolithic catalyst. *Environ. Sci. Pollut. Res.* **2021**. [[CrossRef](#)] [[PubMed](#)]